



HAL
open science

Projected constraints on scalarization with gravitational waves from neutron star binaries

Laura Sampson, Nicolás Yunes, Neil Cornish, Marcelo Ponce, Enrico Barausse, Antoine Klein, Carlos Palenzuela, Luis Lehner

► **To cite this version:**

Laura Sampson, Nicolás Yunes, Neil Cornish, Marcelo Ponce, Enrico Barausse, et al.. Projected constraints on scalarization with gravitational waves from neutron star binaries. *Physical Review D*, 2014, 90, 10.1103/PhysRevD.90.124091 . insu-03645229

HAL Id: insu-03645229

<https://insu.hal.science/insu-03645229>

Submitted on 28 Apr 2022

HAL is a multi-disciplinary open access archive for the deposit and dissemination of scientific research documents, whether they are published or not. The documents may come from teaching and research institutions in France or abroad, or from public or private research centers.

L'archive ouverte pluridisciplinaire **HAL**, est destinée au dépôt et à la diffusion de documents scientifiques de niveau recherche, publiés ou non, émanant des établissements d'enseignement et de recherche français ou étrangers, des laboratoires publics ou privés.

Projected constraints on scalarization with gravitational waves from neutron star binaries

Laura Sampson,¹ Nicolás Yunes,¹ Neil Cornish,¹ Marcelo Ponce,² Enrico Barausse,^{3,4}
 Antoine Klein,⁵ Carlos Palenzuela,⁶ and Luis Lehner^{7,8}

¹*Department of Physics, Montana State University, Bozeman, Montana 59717, USA*

²*Department of Physics, University of Guelph, Guelph, Ontario N1G 2W1, Canada*

³*CNRS, UMR 7095, Institut d'Astrophysique de Paris, 98bis Boulevard Arago, 75014 Paris, France*

⁴*Sorbonne Universités, UPMC Université Paris 06, UMR 7095,*

98bis Boulevard Arago, 75014 Paris, France

⁵*Department of Physics and Astronomy, The University of Mississippi, University, Mississippi 38677, USA*

⁶*Canadian Institute for Theoretical Astrophysics, Toronto, Ontario M5S 3H8, Canada*

⁷*Perimeter Institute for Theoretical Physics, Waterloo, Ontario N2L 2Y5, Canada*

⁸*CIFAR, Cosmology and Gravity Program, Toronto, Ontario M5G 1Z8, Canada*

(Received 29 July 2014; published 30 December 2014)

Certain scalar-tensor theories have the property of endowing stars with scalar hair, sourced either by the star's own compactness (spontaneous scalarization) or, for binary systems, by the companion's scalar hair (induced scalarization) or by the orbital binding energy (dynamical scalarization). Scalarized stars in binaries present different conservative dynamics than in general relativity, and can also excite a scalar mode in the metric perturbation that carries away dipolar radiation. As a result, the binary orbit shrinks faster than predicted in general relativity, modifying the rate of decay of the orbital period. In spite of this, scalar-tensor theories can pass existing binary pulsar tests, because observed pulsars may not be compact enough or sufficiently orbitally bound to activate scalarization. Gravitational waves emitted during the last stages of compact binary inspirals are thus ideal probes of scalarization effects. For the standard projected sensitivity of advanced LIGO, we here show that, if the neutron star equation of state is such that the stars can be sufficiently compact that they enter the detector's sensitivity band already scalarized, then gravitational waves could place constraints at least comparable to binary pulsars. If the stars dynamically scalarize while inspiraling in band, then constraints are still possible provided the equation of state leads to scalarization that occurs sufficiently early in the inspiral, roughly below an orbital frequency of 50 Hz. In performing these studies, we rederive an easy-to-calculate data analysis measure, an integrated phase difference between a general-relativistic and a modified signal, and connect it directly to the Bayes factor, showing that it can be used to determine whether a modified gravity effect is detectable. Finally, we find that custom-made templates are equally effective as model-independent, parametrized post-Einsteinian waveforms at detecting such modified gravity effects at realistic signal-to-noise ratios.

DOI: [10.1103/PhysRevD.90.124091](https://doi.org/10.1103/PhysRevD.90.124091)

PACS numbers: 04.30.-w, 04.50.Kd, 04.25.-g, 97.60.Jd

I. INTRODUCTION

When gravitational waves (GWs) are detected by second-generation detectors [such as advanced LIGO (aLIGO) [1–3], advanced Virgo (aVirgo) [4,5], and KAGRA [6]] some time in the next few years, one of the most exciting prospects is using these signals to test general relativity (GR) in the very strong-field, *dynamical*, and *nonlinear* regime [7]. There has been much work done on constraining departures from GR dynamics with Solar System and binary pulsar observations, and quite strong bounds have been placed on deviations from Einstein's theory in certain regimes. In particular, the strength of dipole radiation from some types of scalar-tensor (ST) theories is already tightly constrained by observations of the rate of decay of the orbital period of binary pulsars [8–12].

There remains, however, a class of ST theories that can escape these constraints. For theories in this class, initially

proposed by Refs. [13,14], the scalar charge of a compact object is dependent upon the gravitational binding energy (or compactness) of the object itself (*spontaneous scalarization*) [13,14], and, if the object is in a binary, upon the orbital binding energy of the binary system (*dynamical scalarization*), a phenomenon discovered in Ref. [15]. Additionally, once a star acquires a scalar charge, it can scalarize its binary companion (*induced scalarization*) [13–17].

These three types of scalarization can be understood in analogy with magnetization [16]. Induced scalarization [13–17] is similar to what occurs in paramagnetism, where the individual magnetic moments of a large collection of atoms align themselves in the presence of a strong, external magnetic field. This alignment induces an overall magnetization of the collection of atoms. In the case of a neutron star (NS) in the presence of an external scalar field, e.g., one supported by its binary companion, the star can develop a scalar field of its own.

Similarly, spontaneous [13,14,16] and dynamical [15,17] scalarization can both be understood in the context of spontaneous magnetization. In this phenomenon, a collection of unaligned magnetic moments will spontaneously align themselves in some direction as the temperature is lowered past a critical point, even in the absence of an external field. This occurs because, when the temperature is low enough, a new energy minimum appears—a broken symmetry state that is associated with a nonzero net magnetization. A similar second-order phase transition occurs as either the compactness of an individual body or the absolute magnitude of the binding energy of a binary system reaches a large enough value. When this happens, the effective potential of the scalar field changes and a new, spontaneously broken minimum appears. This forces the scalar field to “roll down” to a nonzero expectation value.

The compactness or binding energy at which this phase transition occurs is a function of the coupling constants of the ST theory. However, the compactness (or the binding energy) of a system, be it an individual NS or a binary, is also a function of the NS’s equation of state (EoS). As a result, whether a system scalarizes or not also depends on the EoS. We will discuss these theories in more detail in Sec. II, but it suffices here to say that scalarization (spontaneous, induced, or dynamical) only occurs in these theories when a particular coupling constant, β_{ST} , is sufficiently large and negative (for a fixed EoS, NS compactness, and orbital separation). More negative values of this parameter result in scalarization for systems with smaller compactnesses and larger orbital separations [13,15,17].

A little-appreciated problem exists for these theories if one wishes β_{ST} to be negative, such that scalarization can occur. References [16,18,19] showed that in a cosmological evolution, $\beta_{\text{ST}} > 0$ forces the ST theory to approach GR exponentially; i.e., GR is an attractor in the theory phase space, and thus the parametrized post-Newtonian (ppN) parameters are exponentially close to their GR values. However, by this same argument, we show in Appendix A that a cosmological evolution with $\beta_{\text{ST}} < 0$ makes GR a repeller, forcing ppN parameters in this theory to deviate from their GR values. A more rigorous, nonlinear analysis linking cosmological scales to galactic and eventually Solar System ones would be useful to draw definitive conclusions, but based on these results, the requirement $\beta_{\text{ST}} < 0$, which would enable scalarization, seems incompatible with Solar System experiments. Regardless, these problems might be avoidable if an external potential (see, e.g., Ref. [20]) is included, with a minimum at small values of the scalar field.

Neglecting the above problems, as done regularly in the literature [11–15,17,21], we can study the effects of scalarization on astrophysical observations of binary systems, such as binary pulsars, and then use these observations to constrain ST theories. If the binary components support a scalar field, then an unequal-mass binary will decay faster than in GR due to the emission of dipolar

radiation by the scalar field [13,14]. Such a decay is stringently constrained by binary pulsar observations [11,12], which can place strong bounds on the existence of dipole radiation, scalarization, and the magnitude of β_{ST} . Using observations of a pulsar-white dwarf binary (J1738 + 0333) and a single-polytrope EoS with polytropic index $\Gamma = 2.34$, Ref. [12] has constrained $\beta_{\text{ST}} \gtrsim -4.75$. Using an APR4 (soft) and an H4 (stiff) EoS, Ref. [21] used the binary pulsar observations of Ref. [12] to constrain $\beta_{\text{ST}} \gtrsim -4.5$ and $\beta_{\text{ST}} \gtrsim -5$ respectively.

Clearly, constraints on β_{ST} depend on the NS EoS. For a given EoS, only certain sufficiently large, negative values of β_{ST} produce spontaneous scalarization. The bounds quoted above are roughly the least negative values of β_{ST} that allow for scalarization, given a particular EoS. For example, Ref. [21] showed that for the pulsar in Ref. [12] with mass $\approx 1.46M_{\odot}$, an APR4 EoS requires $\beta_{\text{ST}} < -4.5$ for scalarization to occur, while an H4 EoS requires $\beta_{\text{ST}} < -5$, precisely the constraints quoted in Ref. [21]. Thus, binary pulsar observations constrain a region in the β_{ST} -EoS space, which means that bounds on β_{ST} can be weakened if one considers stiffer EoSs that lead to less compact stars (larger radius given a fixed mass). Additionally, binary pulsars that have been observed thus far are very widely separated (typical separation larger than 10^5 km), and so their orbital binding energy is not large enough to activate dynamical scalarization.

The GWs emitted during the late inspiral of NS binaries may also allow for constraints on scalarization, as these waves are produced when the orbital binding energy is very large and, like binary pulsars, GW observations are extremely sensitive to the orbital decay rate. In this paper, we investigate such an idea by

- (i) constructing an analytical model of the GWs emitted during late NS inspirals in ST theories,
- (ii) calculating the response function of interferometric detectors to such waves in the time and frequency domains through the stationary phase approximation (SPA), and
- (iii) carrying out a detailed, Bayesian parameter estimation and model-selection study, assuming a GW detection with second-generation detectors (in the currently planned configuration).

One of our main results is the following.

GWs emitted in the late inspiral of NS binaries can be used to place constraints on ST theories that are comparable to binary pulsar ones, provided at least one binary component is sufficiently compact to be already spontaneously scalarized by the time the emitted GWs enter the detectors’ sensitivity band.

Second-generation detectors, like aLIGO, aVirgo, and KAGRA, will be sensitive to GWs emitted by binaries with orbital frequencies above ~ 5 Hz. If a NS in a binary is sufficiently compact, for a given EoS and value of β_{ST} , to be already spontaneously scalarized by the time the binary

crosses this frequency threshold, then a GW observation consistent with GR can be used to rule out the existence of dipole radiation and constrain the magnitude of β_{ST} . For example, given a polytropic EoS and a NS binary with (gravitational) masses $(1.4074, 1.7415)M_{\odot}$, a single GW observation consistent with GR at a signal-to-noise ratio (SNR) of 15 would allow us to place the constraint $\beta_{\text{ST}} \gtrsim -4.5$. This constraint is similar in strength to that obtained with current binary pulsar observations and polytropic EoSs [12], but it is complementary in that it derives from sampling the dynamical and nonlinear regime of the gravitational interaction.

Another main result of this paper is the following.

Dynamical scalarization in the late inspiral of NS binaries will be difficult to constrain with GWs, unless the system scalarizes at a low enough orbital frequency (i.e., large enough orbital separation) that a sufficient amount of SNR is accumulated while the ST modifications are active.

Reference [22] proved that an abrupt activation of dipolar radiation can only be observed with GWs emitted by binaries if it occurs at an orbital frequency well below 50 Hz, assuming an aLIGO-type detector and a SNR of 10. Such a threshold frequency corresponds to an orbital separation larger than roughly $35m$, where m is the total mass of the NS binary, or alternatively, ≈ 150 km for a binary with total mass $3M_{\odot}$. Dynamical scalarization at such large separations only happens for quite specific, finely tuned binary systems given realistic NS EoSs and values of β_{ST} not already ruled out by binary pulsar observations [12]. In this analysis, only three systems, out of a total of 80 examined, underwent dynamical scalarization at orbital frequencies below 100 Hz. Of these three, only one exhibited ST effects that were strong enough to detect with aLIGO at a SNR of 15.

We additionally analyze whether another signature of dynamical scalarization—an early plunge once the scalar field activates—is detectable with aLIGO-like detectors. We find the following:

Early plunge and merger due to dynamical scalarization is detectable for certain frequency ranges using model-independent templates.

We modeled the early plunge through a *toy model*, a Heaviside truncation of the GW Fourier amplitude. For this truncation to be detectable, we find that it must occur between orbital frequencies of roughly 45 and 150 Hz, assuming a SNR 15 if no truncation was present. For plunges that occur at lower frequencies, not enough signal would be present in the detector’s sensitivity band to lead to a detection in the first place. For plunges that occur at higher frequencies, the detector’s noise is already large enough that such a plunge is difficult to detect.

The analysis described above required a Markov-chain Monte Carlo (MCMC) mapping of the likelihood surface

to obtain posteriors and Bayes factors (BFs) between a GR and a non-GR model, given a scalarized GW injection, all of which is computationally expensive. Thus, another important result of this paper is the following.

We rederive a computationally inexpensive, data analysis measure to determine whether modified gravity effects are detectable, which we call the *effective cycles of phase*. For the first time, we connect this quantity directly to the Bayes factor. We find that roughly 4 cycles are needed for a modified gravity effect to be detectable at SNR 15.

First derived in [23], the effective cycles are defined as a certain noise-weighted integral of the GW amplitude and the phase difference between a GR and a non-GR inspiral. This measure is inspired by the *useful cycles of phase*, introduced in Ref. [24], but it differs from this quantity in that the BF can be estimated *analytically* in terms of effective cycles. Therefore, the effective cycles are directly connected to an important data analysis measure of detectability in model hypothesis testing.

The effective cycles are a noise-weighted dephasing measure that is ideal for studying the distinguishability between models. A non-noise-weighted dephasing is not a good measure, in spite of being often used in theoretical studies, e.g., [25–27]. The effective cycles take into account the fact that, for departures from GR to be detectable, they must occur in a frequency range in which sufficient SNR is accumulated. This is particularly difficult for GR departures that only become significant at kHz frequencies.

Another question that arose while we carried out this analysis was whether custom-made waveforms are necessary to detect the effects of ST gravity, or whether model-independent templates are sufficient. This question, of course, is SNR dependent, and as explained above, dynamical scalarization is not easily measurable with the SNRs expected in advanced detectors, except in a few cases. Moreover, it is very difficult to develop analytical templates that accurately model the effects of dynamical scalarization. We therefore consider the detectability of spontaneous/induced scalarization effects with custom-made versus model-independent templates, and obtain the following result.

More complicated, model-dependent templates are found to be comparably efficient at detecting GR deviations as the simplest, model-independent waveforms one can construct.

As a proxy for model-independent templates, we use the parametrized post-Einsteinian (ppE) approach of Ref. [28]. The simplest version of such waveforms includes only leading post-Newtonian (PN) order modifications to GR in the waveform; thus, they do not contain the precise PN sequence of terms that a custom-made ST theory template (or signal) would possess. This additional structure should allow custom-made templates to be more effective at detecting GR

deviations present in the signals they are designed to capture. The enhancement leads to an increased detection efficiency at very high SNR, but negligible effects for signals with SNRs we expect to observe. Additionally, we find that more complicated ppE templates, such as those that include a step function in the phase to activate a modified gravity effect above a certain frequency, are as effective as the simplest ppE models at detecting ST-type GR deviations. These results are consistent with those in Ref. [29].

The rest of this paper presents the details of the results described above and is organized as follows. In Sec. II, we give an introduction to the non-GR models of interest in this paper. Next, in Sec. III, we describe in detail the methods we used to develop the waveforms tailored to these models. Then, in Secs. IV and V, we address the question of detectability using effective cycles and a Bayesian analysis respectively. In the final section of this paper, Sec. VI, we conclude and point to future research. Throughout this paper, latin letters refer to spatial indices, greek letters refer to spacetime indices, and we use geometric units in which $G = c = 1$. Additionally, all masses quoted refer to gravitational mass and, unless otherwise specified, we employ the term “spontaneously scalarized” binary (or signal) to refer to binaries (or signals arising from binaries) whose components undergo spontaneous or induced scalarization. We do so because a necessary condition for induced scalarization to happen is the presence of at least one spontaneously scalarized star. The term “dynamically scalarized” binary (or signal) will denote binaries (or signals arising from binaries) that undergo dynamical scalarization.

II. INTRODUCTION TO SCALAR-TENSOR THEORIES

In this section, we briefly describe the theory we will study. Initially presented in Refs. [13,14], this theory has recently been revisited in the context of compact binary inspirals and mergers in Refs. [15,17,21]. Here, we review the basics of this theory, following mainly the presentation of Ref. [17].

A. Basics

Generic ST theories are defined by the Jordan-frame action

$$S = \int d^4x \frac{\sqrt{-g}}{2\kappa} \left[\phi R - \frac{\omega(\phi)}{\phi} \partial_\mu \phi \partial^\mu \phi \right] + S_M[\chi, g_{\mu\nu}], \quad (1)$$

where $\kappa = 8\pi G$, ϕ is a scalar field, R is the Ricci scalar associated with the Jordan-frame metric, $g_{\mu\nu}$, and χ are additional matter degrees of freedom that couple directly to the metric.

The function, $\omega(\phi)$, defines the particular ST theory in play [in some cases there is also a potential function, $V(\phi)$,

but here this potential is set to zero]. For example, Fierz-Jordan-Brans-Dicke (FJBD) theory [30–32] is defined by this action with $\omega(\phi) = \omega_{\text{BD}} = \text{const}$. In this paper, we will consider the class of theories studied in [13,14], which are defined by the action of Eq. (1) with

$$\omega(\phi) = -\frac{3}{2} - \frac{\kappa}{4\beta \log \phi}, \quad (2)$$

where β is a dimensional constant, related to the dimensionless coupling constant of the theory, β_{ST} , by $\beta = (4\pi G)\beta_{\text{ST}}$. The asymptotic value of ϕ at spatial infinity, together with the value of β_{ST} , controls the magnitude of the modifications to GR.

The Jordan-frame action of Eq. (1) can be rewritten in the “Einstein frame” via

$$S = \int d^4x \sqrt{-g^E} \left(\frac{R^E}{2\kappa} - \frac{1}{2} g_{\mu\nu}^E \partial_\mu \psi \partial_\nu \psi \right) + S_M[\chi, g_{\mu\nu}^E / \phi(\psi)], \quad (3)$$

where the Einstein-frame metric is related to the Jordan-frame one via $g_{\mu\nu}^E = \phi g_{\mu\nu}$. The Einstein-frame scalar field ψ is related to its Jordan-frame counterpart via

$$\left(\frac{d \log \phi}{d\psi} \right)^2 = \frac{2\kappa}{3 + 2\omega(\phi)}. \quad (4)$$

In the theories of interest in this paper, this differential equation can be solved to obtain

$$\phi = \exp(-\beta\psi^2), \quad (5)$$

choosing $\psi = 0$ when $\phi = 1$. Using this equation in Eq. (4), one finds

$$\psi[\omega(\phi)] = \frac{1}{2|\beta|} \left[\frac{2\kappa}{3 + 2\omega(\phi)} \right]^{1/2}. \quad (6)$$

In the Einstein frame, the field equations for the metric and the equations of motion for the scalar field are

$$G_{\mu\nu}^E = \kappa(T_{\mu\nu}^\psi + T_{\mu\nu}^{M,E}), \quad (7)$$

$$\square^E \psi = -\beta\psi T^{M,E}, \quad (8)$$

where we have defined

$$T_{\mu\nu}^\psi = \partial_\mu \psi \partial_\nu \psi - \frac{1}{2} g_{\mu\nu}^E g_E^{\alpha\beta} \partial_\alpha \psi \partial_\beta \psi, \quad (9)$$

and $T^{M,E}$ is the Einstein-frame trace of $T_{\mu\nu}^{M,E} = T_{\mu\nu}^M / \phi$, the matter stress-energy tensor in the Einstein frame.

Because of the field redefinition to Einstein-frame variables, the stress-energy tensor conservation $\nabla_\mu T_M^{\mu\nu} = 0$ becomes

$$\nabla_{\mu}^E T_{E}^{\mu\nu} = \beta \psi T_{E} g_{E}^{\mu\nu} \partial_{\mu} \psi, \quad (10)$$

which also follows from the field equations (7) and (8). This equation implies, in particular, that test particles (i.e., point particles with negligible mass) do *not* follow geodesics of the Einstein-frame metric $g_{\mu\nu}^E$, although they do follow geodesics of the original Jordan-frame metric $g_{\mu\nu}$. This means that the weak equivalence principle (i.e., the universality of free fall for weakly gravitating bodies) is satisfied in these theories. Nevertheless, as will become clearer in the next section, the strong version of the equivalence principle (i.e., the universality of free fall for strongly gravitating bodies) is *not* satisfied in scalar-tensor theories. This is because of the presence of “scalar charges” for strongly gravitating bodies, whose appearance can be ultimately traced to the right-hand side of Eq. (10) having a nonzero value.

Solar System tracking of the Cassini spacecraft implies the constraint $w_{\text{BD}} > w_{\text{Cassini}} \equiv 4 \times 10^4$ [33,34] on FJBD theory. Because the class of ST theories that we consider reduces to FJBD in the Solar System [with $\omega_{\text{BD}} = \omega_0$ related to the asymptotic value of ψ , which we denote by ψ_0 , via Eqs. (2) and (5)], this translates into the bound

$$\psi_0 \equiv \frac{1}{2|\beta|} \left(\frac{2\kappa}{3 + 2\omega_0} \right)^{1/2} \lesssim 1.26 \times 10^{-2} \frac{G^{1/2}}{|\beta|}. \quad (11)$$

Binary pulsar observations of the orbital decay rate also constrain the theory, since dipolar radiation would greatly accelerate the inspiral [12,35]. These observations require that $\beta_{\text{ST}} \gtrsim -4.75$ [12], but as discussed in the Introduction, this constraint depends on which EoS is used [21].

B. Time-domain scalar charges

Given a binary system that consists of two bodies of masses m_1 and m_2 , the evolution of the GWs emitted by this binary will depend on the scalar charges of the two bodies, α_1 and α_2 . In turn, these charges depend on $\beta_{\text{ST}} \equiv \beta/(4\pi G)$, but also on the NS compactness C and, in a binary in quasicircular motion, on the (magnitude of their) orbital velocity v (equivalently, their separation or their orbital frequency). It is therefore necessary to have a good analytic representation of these charges as a function of β_{ST} , C , and v , in order to construct accurate SPA templates.

The scalar charges are defined by [13]

$$\alpha_A = -\frac{1}{\sqrt{4\pi G}} \frac{\partial \ln m_A^E(\psi)}{\partial \psi}, \quad (12)$$

where $m_A(\psi)$ is the mass parameter that enters the point-particle action in the Einstein frame. A related quantity, the *sensitivity*, s_A , can be similarly defined by [36]

$$s_A = \frac{\partial \ln m_A(\phi)}{\partial \ln \phi}, \quad (13)$$

where $m_A(\phi)$ is the mass parameter that enters the point-particle action in the Jordan frame. These derivatives are to be taken by keeping the baryonic mass fixed, and the two masses are related via $m_A^E = m_A \phi(\psi)^{-1/2}$. The sensitivities and the scalar charges are then related by [17,37,38]

$$\alpha_A = -\frac{2s_A - 1}{\sqrt{3 + 2\omega_0}}, \quad (14)$$

where ω_0 must be greater than 4×10^4 due to the Cassini bound [33,34].

In a FJBD theory with a given ω_{BD} , the scalar charges (and thus the sensitivities) are parameters determined exclusively by the compact object’s EoSs. Will and Zaglauer [39] found that in this theory the sensitivities are in the interval (0.1,0.3) for NSs, becoming 0.5 in the black hole limit. Of course, the scalar charges in this theory are much smaller than the sensitivities, as the former are suppressed by $\approx \omega_0^{-1/2}$ relative to the latter. Fixing the EoS, the sensitivities depend only on the mass of the object. Thus, since NS masses are expected to be in the range (1, 2.5) M_{\odot} , NS binaries have $s_1 \approx s_2$, and dipole radiation is suppressed [39]. Such suppression explains why it would be difficult to observe or constrain dipole radiation from GWs emitted during binary NS inspirals within FJBD theory.

In the ST theories of Refs. [13,14], however, the scalar charges can be spontaneously/dynamically generated. In this process of scalarization, the charges can be excited once the gravitational energy of the system exceeds a certain threshold. In isolation, this energy is simply proportional to the NS compactness, $C = M/R$, the ratio of the NS mass to its radius. When in a binary, this energy is not only due to the individual compactnesses, but also to the binding energy of the system, which scales as $m_1 m_2 / r_{12}$, with (m_1, m_2) the NS masses, and r_{12} the orbital separation.

The behavior of the scalar charges during the inspiral and plunge of a NS binary has so far only been calculated semianalytically in Ref. [17] for a polytropic EoS with exponent $\Gamma = 2$ and maximum NS gravitational mass of $1.8M_{\odot}$, and these results have been validated by comparing the binary’s orbital evolution to the fully nonlinear simulations of Ref. [15]. Using the results of Ref. [17], Fig. 1 shows the scalar charge for the more massive star in a NS binary system with $(m_1, m_2) = (1.4074, 1.7415)M_{\odot}$ as a function of the dominant GW frequency f (twice the orbital frequency for a quasicircular binary) up to contact for ST theories with $\beta_{\text{ST}} = -3.0, -3.25, -3.5$, and -4.5 .

As noted, the construction of a SPA waveform in ST theories will require a parametrization of these scalar

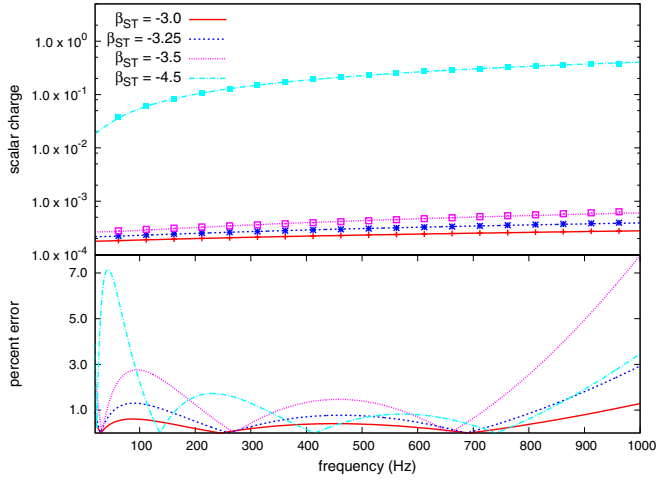


FIG. 1 (color online). The upper panel shows the scalar charges for a $1.7415M_{\odot}$ NS with a $1.4074M_{\odot}$ companion, for various values of β_{ST} and as a function of GW frequency. The actual data are shown with symbols, and the fits to the data by the different line styles. In the lower panel, we plot the percentage error between the data and the fits. Observe that this error never exceeds $\approx 7\%$.

charges as a function of β_{ST} , m_A , and v . We desire an analytic expression for the scalar charges because, when calculating the Fourier transform of the GW phase in the SPA, we need to analytically compute *indefinite* integrals of functions of these charges. Thus motivated, we will use the following fitting function:

$$\alpha_A = \sum_{i=0}^{i_{\text{max}}} a_i^{(A)} v^i, \quad (15)$$

where $v \equiv (\pi m f)^{1/3}$, with f the dominant GW frequency (twice the orbital frequency), and the coefficients $a_i^{(A)}$ are functions of $(m_A, m, \beta_{\text{ST}})$. We further expand these coefficients as polynomials:

$$a_i^{(A)} = \sum_{j=0}^{j_{\text{max}}} \sum_{k=0}^{k_{\text{max}}} \sum_{\ell=1}^{\ell_{\text{max}}} (a_{ijk\ell}^{(A)}) (-\beta_{\text{ST}})^{\ell} m_A^j m^k. \quad (16)$$

The more terms kept in the sum, of course, the more closely the function approximates the numerical data. We find empirically that the choice $i_{\text{max}} = l_{\text{max}} = 2$ and $j_{\text{max}} = k_{\text{max}} = 3$ suffices for our purposes, which leads to $2 \times 3 \times 3 = 18$ fitting coefficients at each PN order.

We use the fitting function described above to fit for the scalar charges as a function of v . First, we use the data from Ref. [17] to numerically construct α_A as a function of v , from a GW frequency of 10 Hz (the beginning of the aLIGO sensitivity band) up to contact, with a fine discretization, for 37 systems with different masses (m_1, m_2) and values of β_{ST} . Each of these data sets is slightly noisy in

the low-frequency regime due to small numerical errors, so before proceeding, we smooth each of them with a moving average algorithm using the nearest ten neighbors.

When carrying out the fits, we do not use the full domain of the data (from $f = 10$ Hz to contact), but rather restrict attention to the low velocity regime. As found in Refs. [40–42], when fitting numerical data to a PN function, the high velocity regime should not be included in the numerical data. This is because this regime would contaminate the fitting coefficients, as they attempt to capture both the low and high velocity behavior of the function. Moreover, one should not use a very high PN order fitting function, as the high PN order terms would contaminate the low PN order ones. For these reasons, we choose $i_{\text{max}} = 2$ and fit in the region (10,800) Hz, which we found empirically to yield robust results, as we will show below.

Finally, in doing the fits, we have neglected scalar charges that undergo dynamical scalarization (i.e., charges that are close to zero when the binary enters the LIGO band at an orbital frequency of 5 Hz, and then grow very quickly later in the inspiral) for the following reason. The SPA calculation requires that we bivariate Taylor expand all quantities in both $v \ll 1$ and in the GR deviation parameter, which in the ST case is α_A . Although $\alpha_A \ll 1$ during the inspiral, $d\alpha_A/d \ln v > 1$ at a certain frequency, around $f = 300$ Hz for the cases considered in Fig. 2. Thus, during dynamical scalarization, one should not expand in derivatives of α_A , which makes any analytic treatment very difficult. Third, a polynomial in velocity is ill suited for representing scalar charges that undergo dynamical

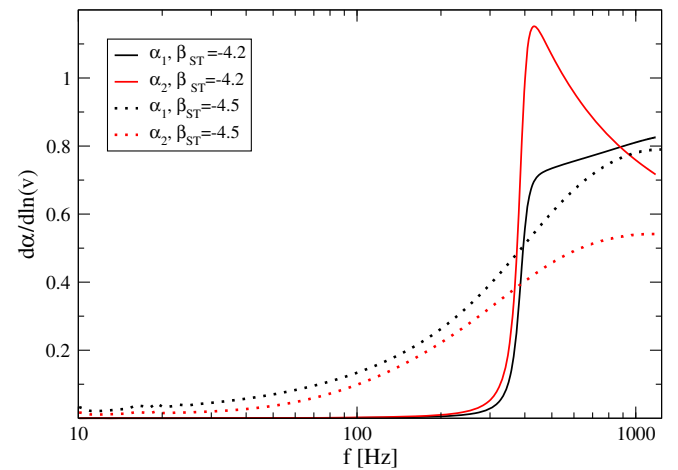


FIG. 2 (color online). Logarithmic derivative of the scalar charges with respect to velocity as a function of GW frequency for a NS binary with masses $(m_1, m_2) = (1.4074, 1.7415)M_{\odot}$ computed with the numerical results presented in Ref. [17]. Observe that the derivative of the charge in the $\beta_{\text{ST}} = -4.25$ case rises very rapidly around $f = 300$ Hz, rapidly exceeding unity. On the other hand, the derivative in the $\beta_{\text{ST}} = -4.5$ case remains smaller than unity during the entire inspiral.

scalarization. If one insisted on using such a fitting function, then the coefficients $a_i^{(A)}$ would grow by factors of 10^3 with increasing i . Such a highly divergent behavior of the fitting coefficients renders any subsequent PN expansion useless.

Given this, we fit Eq. (15) independently to each set of clean data corresponding to a *particular* value of β_{ST} rather than fitting all the data with the same set of coefficients at the same time. We proceed this way because the scalar charges for larger values of $|\beta_{\text{ST}}|$ (i.e., $\beta_{\text{ST}} = -4.5$) are much larger than, for example, the charges at $\beta_{\text{ST}} = -3.5$. This, paired with our lack of data for values of $|\beta_{\text{ST}}| < 3.0$ and the sparseness of the data in (m_1, m_2) space, causes our algorithm to generate poor fits for small values of β_{ST} . In particular, the fitting function obtained by simultaneously fitting all the data does not monotonically approach zero as $\beta_{\text{ST}} \rightarrow 0$. We therefore arrive at a set of $n = 18$ coefficients at each PN order for each different value of β_{ST} . Figure 1 shows the fitted function and the numerical data for several values of β_{ST} , where we note that the error in the fit never exceeds 7% in the frequency window $[10:10^3]$ Hz.

III. DEVELOPING WAVEFORMS FOR SCALAR-TENSOR THEORIES

In this section, we describe how to construct the time-domain response of the aLIGO detectors to impinging GWs. We use the restricted PN approximation, following mostly the presentation in Refs. [43,44]. We then construct the frequency-domain, SPA waveforms from these time-domain functions, and discuss their regimes of validity.

A. Time-domain response

The response of a GW interferometer to a signal can be computed by investigating how the metric perturbation affects the geodesic deviation. Doing so, one finds [45,46]

$$h(t) = F_+ h_+ + F_\times h_\times + F_b h_b + F_L h_L + F_{\text{se}} h_{\text{se}} + F_{\text{sn}} h_{\text{sn}}. \quad (17)$$

The quantities $(F_+, F_\times, F_b, F_L, F_{\text{se}}, F_{\text{sn}})$ are beam- or angular-pattern functions that depend on the geometry of the detector [see, e.g., Eqs. (2)–(7) in Ref. [44]]. The quantities $(h_+, h_\times, h_b, h_L, h_{\text{se}}, h_{\text{sn}})$ are the six possible GW polarizations in a generic theory of gravity: the plus mode, the cross mode, the scalar “breathing” mode, the scalar “longitudinal” mode, and the two vector modes. Recall that GR, being a massless spin-2 theory, has only two propagating degrees of freedom.

The waveform polarizations can be computed from the trace-reversed metric perturbation in the far zone (at a distance much greater than a GW wavelength from the center of mass of the binary) via

$$h_+ = e_{ij}^+ \left(P_m^i P_l^j \bar{h}^{ml} - \frac{1}{2} P^{ij} P_{ml} \bar{h}^{ml} \right), \quad (18)$$

$$h_\times = e_{ij}^\times \left(P_m^i P_l^j \bar{h}^{ml} - \frac{1}{2} P^{ij} P_{ml} \bar{h}^{ml} \right), \quad (19)$$

$$h_b = \frac{1}{2} (\hat{N}_{jk} \bar{h}^{jk} - \bar{h}^{00}), \quad (20)$$

$$h_L = \hat{N}_{jk} \bar{h}^{jk} + \bar{h}^{00} - 2\hat{N}_j \bar{h}^{0j}, \quad (21)$$

$$h_{\text{sn}} = e_k^x [P_j^k (\hat{N}_i \bar{h}^{ij} - \bar{h}^{0j})], \quad (22)$$

$$h_{\text{se}} = e_k^y [P_j^k (\hat{N}_i \bar{h}^{ij} - \bar{h}^{0j})], \quad (23)$$

where we use multi-index notation $\hat{N}^{l_1 \dots l_n} = \hat{N}^{l_1} \dots \hat{N}^{l_n}$. Here, \hat{N}^i is a unit vector pointing from the source to the detector, $P_{ij} = \delta_{ij} - \hat{N}_{ij}$ is a projection operator orthogonal to \hat{N}^i , and e_i^x and e_i^y are basis vectors orthogonal to \hat{N}^i . If we choose a coordinate system defined by the triad $(\hat{i}^i, \hat{j}^i, \hat{k}^i)$, such that \hat{N}^i is given by

$$\hat{N}^i = \sin \iota \hat{j}^i + \cos \iota \hat{k}^i, \quad (24)$$

then

$$e_x^i = -\hat{i}^i, \quad (25)$$

$$e_y^i = \cos \iota \hat{j}^i - \sin \iota \hat{k}^i, \quad (26)$$

$$e_{ij}^+ = \frac{1}{2} (e_i^y e_j^y - e_i^x e_j^x), \quad (27)$$

$$e_{ij}^\times = \frac{1}{2} (e_i^x e_j^y + e_i^y e_j^x), \quad (28)$$

where ι is the inclination angle, such that $\hat{L}^i \hat{N}_i = \cos \iota$, with \hat{L}^i the unit orbital angular momentum vector.

The ST theories of Refs. [13,14] have, in principle, three propagating GW modes: the two transverse-traceless modes (h_+ and h_\times) and the breathing mode (h_b). In the Eardley *et al.* classification [47], these modes correspond to the excitation of the Newman-Penrose scalars Ψ_4 and Φ_{22} . One can show [15], however, that Φ_{22} is proportional to ψ_0 (or alternatively to $\omega_0^{-1/2}$) to leading order in a $\psi_0 \ll 1$ expansion; Ψ_4 is, of course, independent of ψ_0 to leading order. Thus, the effect of h_b in the response $h(t)$ is subleading in ψ_0 relative to the effect of h_+ and h_\times [15]. In fact, this is exactly the same as in standard FJBD theory [48,49]. Even if this were not the case and the response to the breathing mode were not suppressed as $1/\sqrt{\omega_0}$, the detectability of this mode would require a network of detectors [44,50–53]. Given this, we will neglect the breathing mode in the response function.

B. Time-domain waveform and the restricted PN approximation

As explained above, the interferometer response is dominated by the plus- and cross-polarized metric perturbations, $h_+(t)$ and $h_\times(t)$, which must be obtained by solving the modified field equations in the PN approximation. In the far zone, these waves can be written as the following PN sum:

$$h_{+,\times}(t) = \frac{2G\eta m}{D_L} x(t) \sum_{p=0}^{+\infty} x(t)^{p/2} H_{+,\times}^{(p/2)}(t), \quad (29)$$

where D_L is the (luminosity) distance from the source to the detector, $\eta = m_1 m_2 / m^2$ is the symmetric mass ratio, and recall that $m = m_1 + m_2$ is the total mass, and $x(t) = [2\pi G_{\text{eff}} m F(t)]^{2/3}$ is the (time-dependent) PN expansion parameter of leading $\mathcal{O}(1/c^2)$, with $F(t)$ the orbital frequency. Notice that x depends on $G_{\text{eff}} \equiv G(1 + \alpha_1 \alpha_2)$, because in these theories the Newtonian force of attraction between two bodies, and thus, Kepler's third law of orbital motion, takes on the usual Newtonian expression, but with the replacement $G \rightarrow G_{\text{eff}}$ [13,39]. Recall that α_1 and α_2 are the scalar charges of NSs, which depend on the internal structure of the bodies and on the gravitational binding energy of the system, as discussed in Sec. II B.

The time functions $H_{+,\times}^{(p/2)}$ can always be written in terms of an amplitude $[A_{+,\times}^{(p/2,n)}(t)$ or $B_{+,\times}^{(p/2,n)}(t)]$ and the binary's orbital phase $\phi(t)$:

$$H_{+,\times}^{(p/2)} = \sum_{n=0}^{\infty} (A_{+,\times}^{(p/2,n)} \cos n\phi + B_{+,\times}^{(p/2,n)} \sin n\phi). \quad (30)$$

To leading PN order (keeping only the $p = 0$ term), the oscillating part of Eq. (29) reduces to

$$h_+(t) = 2\mathcal{A}(t)(1 + \cos^2 \iota) \cos 2\phi(t), \quad (31)$$

$$h_\times(t) = -4\mathcal{A}(t) \cos \iota \sin 2\phi(t). \quad (32)$$

Here, we have defined the time-dependent amplitude

$$\mathcal{A}(t) = -\frac{\mathcal{M}}{D_L} [2\pi G m F(t)]^{2/3}, \quad (33)$$

with $\mathcal{M} = \eta^{3/5} m$ the chirp mass, and ι is the inclination. Notice that this is functionally exactly the same result as in GR, because, as discussed in Sec. III A, ST corrections to the amplitude scale as ψ_0 , and are thus subleading.

The *restricted PN approximation* consists of approximating the time-domain waveform by the leading PN order terms in the waveform amplitudes, without restricting the PN order in the waveform phase. That is, one keeps only the leading, $p = 0$ term in Eq. (29), thus obtaining

Eqs. (31) and (32), but as many PN terms as one wishes in the orbital phase $\phi(t)$. Such an approximation is reasonable in a first analysis because interferometric detectors are much more sensitive to the phase of the response than the amplitude.

The plus- and cross-polarized metric perturbations in ST theories, and thus the time-domain interferometric response, are different from those predicted by GR mainly because of the temporal evolution of the orbital phase. The phase can be obtained by integrating the expression

$$\dot{\phi} = 2\pi \dot{F} = 2\pi \frac{dE_b}{dt} \left(\frac{dE_b}{dF} \right)^{-1} \quad (34)$$

twice, where E_b is the gravitational binding energy. By the balance law, dE_b/dt must equal (minus) the luminosity \mathcal{L} of all propagating degrees of freedom in the far zone. In GR, the only energy loss is due to the emission of GWs, but in ST theories one must also account for dipolar radiation induced by the propagation of the scalar mode:

$$\mathcal{L} = \frac{G}{3} \eta^2 (\alpha_1 - \alpha_2)^2 x^4 + \frac{32}{5} G \eta^2 x^5, \quad (35)$$

where the first term is due to dipole radiation and the second due to quadrupolar radiation. We then see that ST theories modify the evolution of the orbital phase, which is precisely the component of the interferometric response that detectors are most sensitive to.

C. Fourier response and the stationary phase approximation

In GW data analysis, one uses the Fourier transform of the response function (the Fourier response), instead of the time-domain response. In computing the frequency- or time-domain response, one can effectively neglect the time dependence of the beam-pattern functions. These are induced by the rotation and motion of the Earth, which occurs on a time scale much longer than the duration of the GW signal, which is typically less than 20 min for the signals that fall in the sensitivity band of second-generation, ground-based detectors, such as aLIGO, aVirgo, and KAGRA. Thus, the Fourier response can be written as

$$\tilde{h}(f) = \int_{-\infty}^{\infty} dt e^{2\pi i f t} [F_+ h_+(t) + F_\times h_\times(t)], \quad (36)$$

where (F_+, F_\times) are effectively constant.

Using the restricted PN approximation [Eqs. (31) and (32)], we can rewrite the Fourier response of Eq. (36) as

$$\tilde{h}(f) = \int_{-\infty}^{\infty} dt e^{2\pi i f t} \mathcal{A}(t) [Q_C \cos 2\phi(t) + Q_S \sin 2\phi(t)], \quad (37)$$

where we have defined the cosine- and sine-projected beam-pattern functions

$$Q_C = 2(1 + \cos^2 i) \cos 2\Psi F_+ - 4 \cos i \sin 2\Psi F_\times, \quad (38)$$

$$Q_S = 2(1 + \cos^2 i) \sin 2\Psi F_+ + 4 \cos i \cos 2\Psi F_\times, \quad (39)$$

with Ψ the polarization angle. For binary systems that are in a quasicircular orbit and whose binary components are not spinning, the inclination angle and $Q_{C,S}$ are all constant. The quasicircular and nonspinning approximations are sufficient for our analysis because most NS binaries are expected to have circularized and spun down by the time they enter the sensitivity band of second-generation, ground-based detectors.

The integral in Eq. (37) that defines the Fourier response falls in the class of generalized Fourier integrals. When the integrands have a stationary point, namely a time t_0 at which $\dot{\phi}(t_0) = \pi f$, the integral can be approximated via the method of steepest descent, which to leading order reduces to the SPA [43,54]. For this approximation to hold, the amplitude of the integrand must be slowly varying, while the phase must be rapidly oscillating, such that the integral is nonvanishing only in a small neighborhood around the stationary point.

Within the SPA, the integral in Eq. (37) reduces to

$$\tilde{h}(f) = \tilde{A} f^{-7/6} e^{i\Psi(f)}, \quad (40)$$

where f is the Fourier or GW frequency (twice the orbital frequency), the Fourier amplitude is a constant given by

$$\tilde{A} \equiv -\left(\frac{5}{384}\right)^{1/2} \pi^{-2/3} \frac{\mathcal{M}^{5/6}}{D_L} (Q_C + iQ_S), \quad (41)$$

and the Fourier phase must be computed from [43,55]

$$\Psi(f) = 2\pi \int^{f/2} dF' \left(2 - \frac{f}{F'}\right) \frac{F'}{\dot{F}(F')}. \quad (42)$$

This expression makes it clear that the dominant ST modifications to the Fourier response are due to modifications to the rate of change of the orbital frequency.

D. SPA templates in scalar-tensor theory

We now follow the analysis of the previous subsection and provide explicit formulas for the Fourier transform in the SPA of restricted PN waveforms in ST theories to 1 PN order. We first focus on the binding energy and its rate of change. The former is presented in Eq. (6.4) of Ref. [38] in terms of the individual masses and velocities of the system. One can transform the binding energy to relative coordinates, through the mapping in Eqs. (6.9)–(6.11) of the same paper. The rate of change of the orbital binding energy is equal to the energy flux carried by all propagating degrees

of freedom by the balance law. This quantity is presented in Eqs. (6.16) and (6.17) of Ref. [38] in relative coordinates.

The ST-theory-modified version of Kepler's third law of motion can be computed by solving $|a^i| = r_{12}\omega^2$ in a PN expansion for r_{12} , the relative orbital separation, using also that $|v_{12}^i| = r_{12}\omega$, where we recall that we are considering only binaries in quasicircular orbits. The relative acceleration a^i is given in Eqs. (1.4) and (1.5) of Ref. [38], where ω is the orbital angular velocity. We find that

$$r_{12} = \frac{m}{x} \left\{ \left(1 + \frac{1}{3}\alpha_1\alpha_2\right) + x \left[\left(\frac{\eta}{3} - 1\right) + \frac{1}{3}\alpha_1\alpha_2(\eta - 1) \right] + \mathcal{O}(x^2, \alpha_A^4) \right\}, \quad (43)$$

where we have set $\psi_0 = 0$, as this quantity is constrained to be less than 10^{-2} by current observations.

With the above modified version of Kepler's third law, one can rewrite the binding energy and its rate of change as a function of the PN expansion parameter. Using the definition of Eq. (34), the rate of change of the orbital frequency is then

$$\begin{aligned} \dot{F} &= \frac{1}{2} \frac{\eta}{\pi m^2} x^{9/2} (\alpha_1 - \alpha_2)^2 \\ &+ \frac{48}{5} \frac{\eta}{\pi m^2} x^{11/2} \left\{ 1 + \frac{1}{576} \left[(-15 - 35\eta)\alpha_1^2 \right. \right. \\ &+ \frac{1}{576} (35\eta + 63)\alpha_1\alpha_2 + \alpha_1\alpha_1' \left(\frac{5}{144}\nu - \frac{5}{48} \right) \\ &\left. \left. - \alpha_1\alpha_2' \left(\frac{5}{144}\nu + \frac{43}{48} \right) + 1 \rightarrow 2 \right] \right\} + \mathcal{O}(x^6, \alpha_A^4), \quad (44) \end{aligned}$$

where $\alpha_A' := d\alpha_A/d \ln v$. The first term in this expression corresponds to dipolar radiation, while the second one is the usual quadrupolar radiation term of GR. Notice that both are corrected by terms proportional to the scalar charges, due to the modification to Kepler's third law.

With all of this at hand, we can now compute the Fourier phase in the SPA through Eq. (42). In Sec. II B, we fitted α_A through Eq. (15), which can be rewritten as

$$\alpha_A = c_A + d_A v + \dots, \quad (45)$$

identifying $a_0^{(A)}$ with c_A and $a_1^{(A)}$ with d_A , which are themselves functions of m_A , m , and β_{ST} . Finally, we find

$$\begin{aligned} \Psi(f) &= 2\pi f t_c - \phi_c - \frac{\pi}{4} + \frac{3}{128\eta v^5} \left[-\frac{5}{168} (c_1 - c_2)^2 v^{-2} \right. \\ &\left. - \frac{8400}{109489} (c_1 - c_2)(d_1 - d_2) v^{-1} + \dots \right]. \quad (46) \end{aligned}$$

We see that the main modification to the Fourier response in the SPA is due to the scalar charges, which induce a

dipole correction to leading order. We have checked that the dipole term is exactly what one obtains in FJBD theory, when one rewrites $c_{1,2}$ in terms of the sensitivities $s_{1,2}$.

The ST-modified Fourier response described above is only valid for systems of *unequal* mass. In the case of equal-mass binaries, the -1 and the -0.5 PN terms in Eq. (46) vanish, because then $s_1 = s_2$. In such a system, the lowest PN order correction to the Fourier phase enters at 0 PN order. Henceforth, we only use the ST-modified SPA for analysis of binaries whose component masses are unequal.

E. Comparison of SPA phase to numerical phase

We can now validate the SPA model of the previous subsection by comparing it to the Fourier transform of the time-domain numerical solutions for the GWs presented in Ref. [17]. Before we do so, we define the measure we will use for such a validation: the dephasing $\Delta\Psi$. This quantity is defined as

$$\Delta\Psi_i = \min_{t_c, \phi_c} |\Psi_{\text{GR}} - \Psi_{\text{ST}}|, \quad (47)$$

where Ψ_{GR} is the Fourier phase in GR, Ψ_{ST} is the Fourier phase in ST theories, and the subindex i labels four different strategies we employ to evaluate Ψ_{GR} and Ψ_{ST} as described below. This measure requires minimization over time and phase of coalescence, i.e., over a constant time and phase shift. Such a minimization is required to compare different template families, e.g., a time-domain waveform to a frequency-domain one.

In order to validate the SPA model of the previous subsection, we will evaluate the dephasing of Eq. (47) in four different ways.

- (1) *Numerical*: Ψ_{GR} and Ψ_{ST} are given by the Fourier transforms of the time-domain GW data of Ref. [17], minimizing the difference over phase and time of coalescence.
- (2) -1 PN: Ψ_{ST} is given by Eq. (46), keeping only the leading PN term (the -1 PN term).
- (3) -0.5 PN: Ψ_{ST} is given by Eq. (46), keeping the leading and first subleading PN terms (the -1 and the -0.5 PN terms).
- (4) 0 PN: Ψ_{ST} is given by Eq. (46), keeping terms up to Newtonian order (the -1 , -0.5 , and 0 PN terms).

In all N PN cases, Ψ_{GR} is the GR Fourier phase in the SPA, for example, given in Refs. [28,56]. By comparing the numerical dephasing to the N PN ones, we will validate the SPA templates constructed in the previous subsection.

Such a comparison is carried out in Fig. 3. The solid line is the numerical dephasing, while the dotted lines are the N PN dephasings in the SPA. Observe that the SPA dephasing at -0.5 PN order is a better approximation than keeping the dephasing to 0 or -1 PN order, relative to the numerical dephasing. We will therefore truncate the fit to the scalar

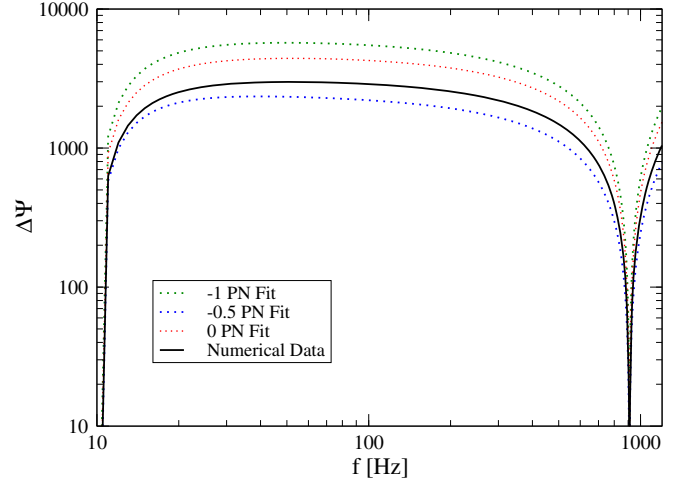


FIG. 3 (color online). Dephasing between a GR and ST signal as a function of GW frequency, calculated using both the numerical Fourier phases (solid curve) and the SPA Fourier phases (dotted curves) for a binary with masses $(1.4074, 1.7415)M_{\odot}$ and $\beta_{\text{ST}} = -4.5$. The ST SPA phases were calculated to various PN orders.

charges at -0.5 PN order for the rest of this paper (i.e., we keep only two ST PN corrections) and model the ST SPA templates by Eq. (46), without ST higher-order PN terms.

F. ppE waveforms

Before proceeding with a detailed data analysis study, we map the SPA templates of Sec. III D to the ppE templates constructed in Ref. [28]. The ppE family is a theory-independent set of templates, designed to capture model-independent deviations from GR with GW observations. This family is constructed by introducing parametrized modifications to both the binding energy and the energy balance equations of GR. Both types of modifications lead to changes in the GW phase, which can be described by introducing a small number of new parameters into the GW template.

The full GW waveform for the coalescence of two compact objects is typically split into three sections: inspiral, merger, and ringdown. ppE templates have been developed for all three phases, but in this paper we are interested only in the inspiral portion. The latter can be defined as the part of the waveform that is generated before the two bodies plunge into each other. The definition of the end of inspiral is somewhat arbitrary, but we follow typical conventions and define the transition from inspiral to merger as occurring at the innermost stable circular orbit of the system in center of mass coordinates (or alternatively at contact). In any case, the merger of NS binaries occurs at the very high-frequency end of aLIGO's sensitivity band, almost outside of it altogether.

The simplest, quadrupole ppE inspiral templates have the form

$$\tilde{h}(f) = \tilde{h}^{\text{GR}} \cdot (1 + \alpha_{\text{ppE}} u^a) e^{i\beta_{\text{ppE}} u^b}, \quad u = (\pi \mathcal{M} f)^{1/3}, \quad (48)$$

where \tilde{h}^{GR} is the Fourier response in GR. These simple ppE waveforms contain an additional amplitude term, $\alpha_{\text{ppE}}u^a$, and an additional phase term, $\beta_{\text{ppE}}u^b$, relative to GR. We refer to α_{ppE} and β_{ppE} as the *strength* parameters of the ppE deviations, and to a and b as the *exponent* parameters.

These ppE waveforms cover all known inspiral waveforms from specific alternative theories of gravity [57] that are analytic in the frequency evolution of the GWs. Some specific examples are discussed in Ref. [7]. They cannot, however, perfectly match the signals generated by the theories of interest in this paper. For the case of induced/spontaneous scalarization, Sec. III E showed that one needs *two* ST PN corrections to the SPA phase (i.e., a -1 and a -0.5 PN term), while the simplest ppE model includes only one. For the dynamically scalarized case, the corrections to the Fourier response are very abrupt (almost a step function), which cannot be captured with a single PN term. In spite of this, we will see that the ppE model is quite adequate at detecting a ST deviation, provided the deviation is strong enough to be detectable in the first case.

IV. DETECTABILITY OF SCALAR-TENSOR DEVIATIONS THROUGH AN EFFECTIVE CYCLES APPROACH

In this section, we carry out the first of a two-part data analysis investigation to determine the detectability of ST deviations in GWs emitted during the late inspiral of NS binaries. We first construct a new, computationally inexpensive data analysis measure to determine when a GR deviation is sufficiently loud for detection with aLIGO-type detectors. We then use this measure on ST signals and ppE signals to estimate their detectability.

A. Useful and effective cycles of phase

Model hypothesis testing, i.e., the determination of whether model A or B is better supported by some data, usually requires a detailed Bayesian analysis through MCMC techniques that map the likelihood surface and the posterior distributions of template parameters in order to calculate BFs.¹ Such studies are computationally expensive, and it is therefore desirable to construct a simple and computationally inexpensive measure for accomplishing

¹The BF, assuming equal priors for the two competing theories, is the odds that one theory is favored by the data over another theory. For instance, a BF of 100 in favor of GR means that there is a 100:1 “betting odds” that GR is the correct theory given the data. In this paper, we are considering only nested models. For example, GR is recovered from ppE templates when the strength parameter $\beta_{\text{ppE}} = 0$. In this case, the BF can be calculated from the Savage-Dickey density ratio, which compares the prior weight at $\beta_{\text{ppE}} = 0$ to the posterior weight at that value. The BF is then calculated via $\text{BF} = p(\beta_{\text{ppE}} = 0|d)/p(\beta_{\text{ppE}} = 0)$. If there is more posterior weight at this point than prior weight, the model-selection process favors GR.

similar goals. The construction of this measure is the topic of this section.

We first describe a quantity that has been used in the literature as a stand-in for the importance of a particular GW phase term [24]: the *useful cycles*, \mathcal{N}_u . This quantity is defined in [24] as

$$\mathcal{N}_u = \left(\int_{F_{\min}}^{F_{\max}} d \ln f \frac{a^2(f)}{S_n(f)} \frac{d\phi}{2\pi df} \right) \times \left(\int_{F_{\min}}^{F_{\max}} d \ln f \frac{a^2(f)}{f S_n(f)} \right)^{-1}, \quad (49)$$

which is essentially a noise-weighted measure of the total number of cycles of phase due to any particular term in the phase evolution. In Eq. (49), $a(f)$ is defined by $|\tilde{h}(f)|^2 = \tilde{A}^2(f) = N(f)a^2(f)/f^2$, with $N(f) = (1/2\pi)(d\phi/d \ln F) = F^2/(dF/dt)$. The expression for \mathcal{N}_u can be reexpressed in terms of the characteristic strain $h_c(f) = \sqrt{f}\tilde{A}(f)$ as

$$\mathcal{N}_u = \text{SNR}^2 \left(\int_{F_{\min}}^{F_{\max}} \frac{h_c^2(f)}{S_n(f)} \frac{1}{N(f)} d \ln f \right)^{-1}. \quad (50)$$

Thus, the number of useful cycles is equal to the harmonic mean of $N(f)$, with a weighting factor equal to the SNR squared per logarithmic frequency interval, $\Delta \text{SNR}^2(f) = h_c^2(f)/S_n(f)$.

The difference in the number of useful cycles between waveform models is sometimes used as a proxy for the detectability of the difference in the models (see, e.g., Refs. [25–27]). One must be very careful when doing this for two reasons. The first is made clear by rewriting Eq. (49) in the form of Eq. (50). This recasting of the useful cycles shows that it is not permissible to simply replace $N(f)$ with $\Delta N(f)$, where $\Delta N(f)$ is the change that is introduced by a particular modification to the phase. In order to calculate \mathcal{N}_u due to a change in the phase evolution, it is necessary to calculate both \mathcal{N}_u from the original phase and from the changed phase, and then take the difference. This is not a problem, *per se*—it is simply an issue that must be kept in mind when calculating \mathcal{N}_u for a particular phase term.

A larger issue with \mathcal{N}_u as a measure of detectability is the murkiness of its connection with quantities such as the BF, which are directly related to model selection. The logarithm of the BF, as derived in Ref. [57], satisfies

$$\log \text{BF} \sim \frac{1}{2}(1 - \text{FF}^2)\text{SNR}^2 + \mathcal{O}[(1 - \text{FF}^2)^2]. \quad (51)$$

We can use the following expression for the fitting factor, FF, given two waveforms with the same amplitude $\tilde{A}(f)$, but with phases that differ by $\Delta\psi(f)$:

$$\text{FF} = \text{SNR}^{-2} \max_{\lambda^a} \left(\int \frac{h_c^2(f) \cos(\Delta\Psi(f))}{S_n(f)} d\ln f \right), \quad (52)$$

where the maximization is done over all system parameters λ^a . In the limit $\text{FF} \sim 1$, i.e., for small deviations from GR, these expressions can be combined to give

$$\log \text{BF} \sim \frac{1}{2} \min_{\lambda^a} \int \frac{h_c^2(f) \Delta\Psi^2(f)}{S_n(f)} d\ln f + \mathcal{O}(\Delta\Psi^4). \quad (53)$$

Given the above expression for the BF, a natural definition for a computationally inexpensive data analysis measure presents itself, the *effective cycles of phase*:

$$\mathcal{N}_e = \min_{\Delta t, \Delta\phi} \left[\frac{1}{2\pi \text{SNR}} \left(\int \frac{h_c^2(f) \Delta\Phi^2(f)}{S_n(f)} d\ln f \right)^{1/2} \right], \quad (54)$$

where $\Delta\Phi \equiv \Delta\Psi(f) + 2\pi f \Delta t - \Delta\phi$, where Δt and $\Delta\phi$ are an arbitrary time and phase shift respectively. As before, the dephasing is $\Delta\Psi = \Psi_1(f) - \Psi_2(f)$, where in our case Ψ_1 will be the Fourier phase of a GR signal and Ψ_2 the phase of a non-GR signal, e.g., for a ppE waveform, $\Delta\Psi(f) = \beta_{\text{ppE}} u^b$. We define \mathcal{N}_e with a $(\Delta t, \Delta\phi)$ minimization because the non-GR terms induce a modification in the frequency and phase evolutions that renders meaningless a direct comparison between time-shift and phase-shift parameters in waveforms living in different theories. Notice, however, that we do not minimize over *all* parameters, as would be required to relate \mathcal{N}_e to the BF. A full minimization procedure is costly and it would involve a MCMC analysis in general, while the minimization with respect to only $(\Delta t, \Delta\phi)$ is inexpensive.

We can now see that this quantity is directly related to model selection through the BF:

$$\log \text{BF} \sim 2\pi^2 \text{SNR}^2 \min_{\lambda^a} \mathcal{N}_e^2. \quad (55)$$

The effective cycles, \mathcal{N}_e , as defined in Eq. (54), i.e., minimized over $(\Delta t, \Delta\phi)$ only, give an *upper limit* to the BF. The fully minimized \mathcal{N}_e will in general be smaller than Eq. (54) due to covariances between system parameters. This means that \mathcal{N}_e is not a perfect proxy for detectability. That is, if \mathcal{N}_e due to a particular term in the phase is large, this may or may not mean that the term is detectable. However, if \mathcal{N}_e due to a particular phase term is small, this *does* indicate that the term will *not* be detectable.

The above is an alternative means of deriving the quantity first derived in [23], which is there referred to as the distinguishability/measurability. Up to some rearranging of various factors, this quantity and the effective cycles of phase are the same. The connection between this quantity and the Bayes factor, though, is a new result.

How are the useful and effective cycles related? From the definitions of \mathcal{N}_u and \mathcal{N}_e , it is clear that the former gives

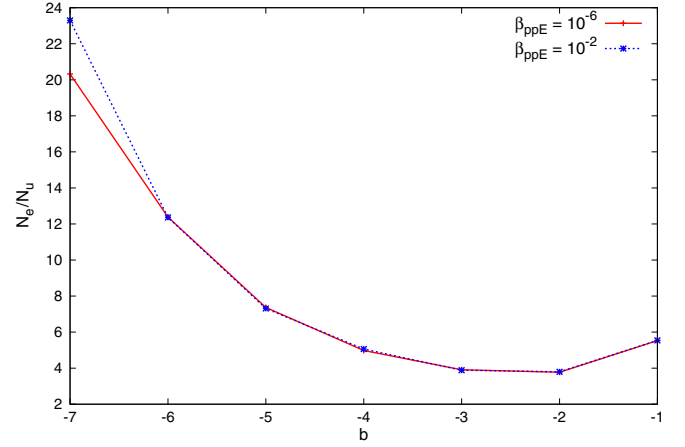


FIG. 4 (color online). The ratio of effective cycles to useful cycles, calculated as a function of b , for two fixed values of β_{ppE} .

the difference in the harmonic mean of the number of cycles, while the latter gives the root-mean-square difference in the number of cycles. This is an important difference— \mathcal{N}_e is directly related to the BF in the small deformation limit. For certain signals, however, the difference can be shown to be a GR-modification-dependent constant factor. To see this, consider inspiral GWs in the PN approximation both in GR and in ppE form. The orbital phase $\phi(f) = 2\pi f t(f) - \Psi(f) - \pi/4$ is a power series in $v = (\pi M f)^{1/3}$, just like the Fourier phase $\Psi(f)$ in both GR and ppE theory. The logarithmic derivative, $d\phi/d\ln f$, preserves the structure of such a power series, and so the PN series for $\Psi(f)$ and for $N(f)$ differ only by b -dependent, order unity factors in each of the coefficients. The relation between \mathcal{N}_e and \mathcal{N}_u is shown in Fig. 4 and derived in Appendix B. Of course, the useful and effective cycles defined here can be computed given *any* form of phase evolution, and thus, they are not restricted to phases in the PN approximation.

B. Useful and effective cycles as a measure of detectability of general non-GR effects

Now that we have introduced the concept of effective cycles, we will use it to determine when a particular GR deviation is detectable. In particular, we will determine the number of useful and effective cycles that are needed for ppE deviations to lead to a BF that favors the ppE model.

We inject ppE signals with varying strength β_{ppE} parameters and exponent b parameters and then

- (i) calculate \mathcal{N}_u and \mathcal{N}_e due to the ppE terms relative to a GR signal ($\beta_{\text{ppE}} = 0$) and
- (ii) run a MCMC analysis to calculate the BF between a ppE model and the GR model.

The second item requires the choice of a prior range for each ppE strength parameter, which we choose to be $|\beta_{\text{ppE}}| \leq 5 \times 10^{-5}$ for $b = -7$, $|\beta_{\text{ppE}}| \leq 5 \times 10^{-4}$ for

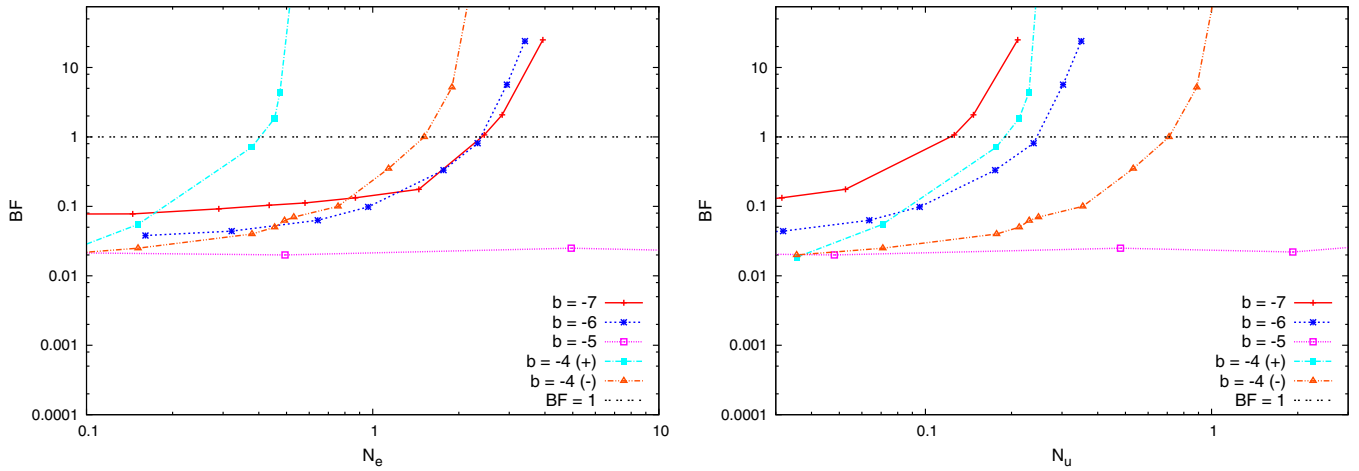


FIG. 5 (color online). BF in favor of a modification to GR versus the number of effective cycles (left) and useful (right) cycles induced by that modification for different types of ppE corrections. For the $b = -4$ cases, the line labeled (-) corresponds to a negative value for β_{ppE} , and the line labeled (+) corresponds to a positive value; all other injections had positive values for β_{ppE} . Observe that the b dependence of the relationship between BF and \mathcal{N}_u is the opposite of what one would expect.

$b = -6$, and $|\beta_{\text{ppE}}| \leq 5$ for $b = -5$ and $b = -4$. These prior ranges were derived by examining the results in Ref. [57] and requiring that the deviations be detectable given a GW signal with $\text{SNR} \approx 10$.

Every injection in this study consists of a $(1.4074, 1.7415)M_{\odot}$, NS/NS, nonspinning binary, with zero inclination angle, and with $\text{SNR} \approx 15$, which corresponds to a luminosity distance $D_L \approx 50$ Mpc. We choose the zero-detuned, high-power spectral noise density projected for aLIGO [58], stopping all integrations at 1000 Hz. This frequency is lower than the GW frequency at which the NSs touch each other, which is approximately between 1250 and 2000 Hz, depending on the NS EoS.

Figure 5 shows the BF on a logarithmic scale versus the absolute value of the number of effective (left panel) and useful (right panel) cycles introduced by signals with different ppE exponent parameters, starting at $b = -7$ (a -1 PN term) and going up to $b = -4$ (a 0.5 PN term). Recall that ST theories lead to modifications at -1 PN order and higher and that a BF larger than 1 indicates the data support the non-GR model. Observe that detectability occurs when \mathcal{N}_u is between 0.1 and 1 and when \mathcal{N}_e is between 2 and 4 cycles of phase for most of the ppE injections. This is not true, however, for the $b = -5$ case, because of the almost perfect correlation between chirp mass \mathcal{M} and β_{ppE} when $b = -5$: a straight line in the two-dimensional \mathcal{M}_c - β_{ppE} plan similar to Fig. 6 in [29]. Because of this, a deviation from GR at the 0 PN (Newtonian) level would have to be very large to be detectable, as previously noted in Ref. [57].

Observe also in Fig. 5 the difference in detectability for phase terms that accumulate either positive or negative cycles of phase. As stated, Fig. 5 shows the *absolute value* of the useful or the effective cycles of phase introduced by each ppE term. For injections made with a positive β_{ppE} , the

actual sign of the cycles of phase is negative. We used this type of injection for most of the lines in this figure, but for the $b = -4$ case, we injected both positive and negative values of β_{ppE} . We find that the positive values are detected more easily than the negative values.

This effect can be understood by examining the posterior distribution of β_{ppE} at $b = -4$, shown in Fig. 6 together with the posterior of β_{ppE} at $b = -7$. Observe that the posteriors are not symmetric about $\beta_{\text{ppE}} = 0$. In the case of $b = -4$, injecting a positive value of β_{ppE} results in no posterior weight at $\beta_{\text{ppE}} = 0$ for much smaller values of $|\beta_{\text{ppE}}|$ than injecting a negative value. The asymmetry in the posterior distributions can again be understood by noting that β_{ppE} is correlated with the mass parameters, which are, of course, forced to be positive.

Figure 5 also shows that the threshold in \mathcal{N}_e for detectability (e.g., the value of \mathcal{N}_e at which the BF equals 10) is lower for terms that are of very high PN order. Comparing the left and right panels of this figure, we observe that the \mathcal{N}_u threshold exhibits the opposite behavior. The \mathcal{N}_e threshold behavior is what one would expect because high PN order terms have small covariances with the ppE strength parameters and the system parameters. It is therefore very difficult for a GR waveform to match the phasing of these types of injections, while the opposite is true for low PN order ppE effects. This fact illustrates the advantage of using \mathcal{N}_e instead of \mathcal{N}_u as a measure of detectability: the $\log(\text{BF})$ as a function of \mathcal{N}_e exhibits the expected behavior as b changes, but $\log(\text{BF})$ as a function of \mathcal{N}_u shows the opposite behavior.

So far, the discussion has assumed a fixed SNR of 15, but clearly the detectability of a GR deviation depends on the SNR of the signal. To understand this, we performed the same analysis as above but with $b = -3$ fixed and signals of differing SNRs. The results are plotted in Fig. 7, where

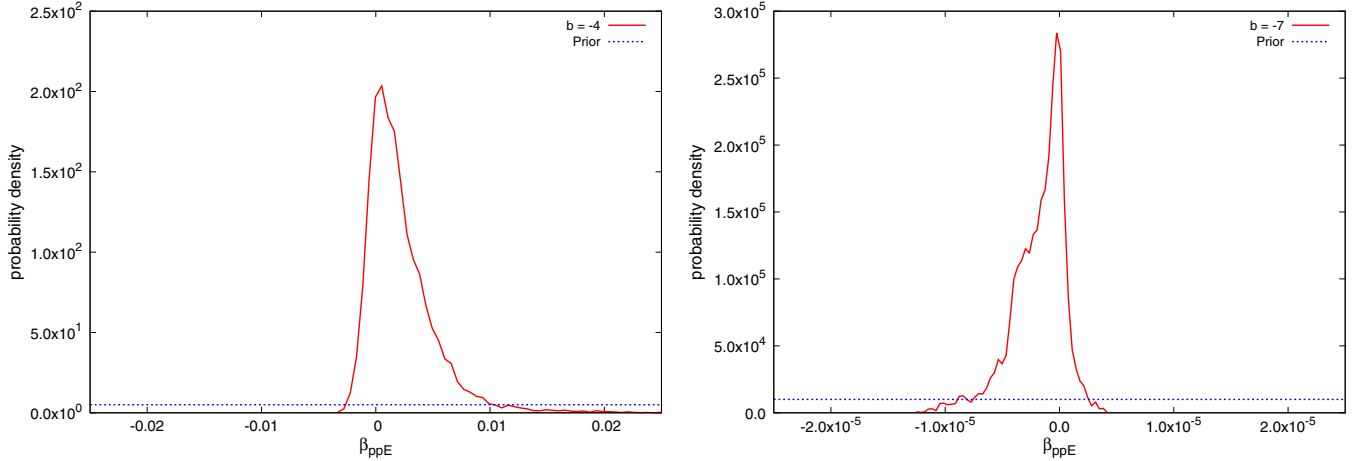


FIG. 6 (color online). Posterior distributions for β_{ppE} for a ppE search template with $b = -4$ (left) and $b = -7$ (right), given a GR injection. Observe that these distributions are not symmetric about zero, which explains why changes to the GW phase of different signs are detectable at different levels.

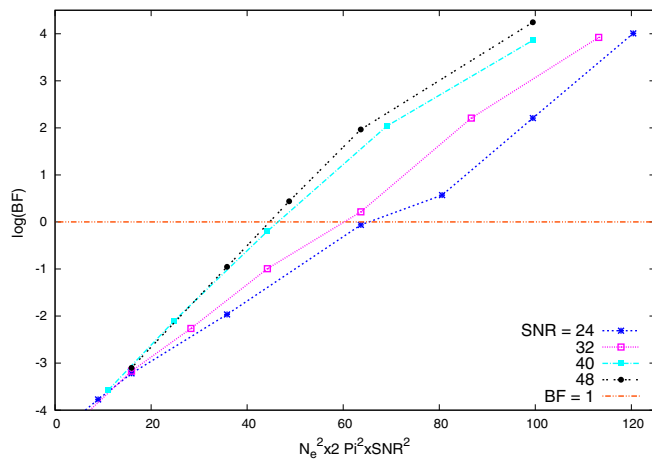


FIG. 7 (color online). The BF in favor of a deviation from GR as a function of effective cycles of phase scaled by their SNR for ppE injections with $b = -3$. Observe the almost linear relation between $\log(\text{BF})$ and $\mathcal{N}_e^2 \text{SNR}^2$, as predicted in Eq. (55).

we observe that the number of effective cycles necessary for a detection of a modification to GR scales approximately as the SNR squared, as expected from Eq. (55). That equation was derived assuming small deviations from GR, but here we see that regardless of the value of the ppE exponent, Eq. (55) is still approximately satisfied.

C. Useful and effective cycles as a measure of detectability of ST effects

We now apply what we have learned about effective cycles to ST theories. First, we must discuss exactly which signals we will analyze in detail. We employ data from Ref. [17], which consist of 80 GW signals from NS binaries with constituent masses ranging from approximately $1.4M_\odot$ to $1.7M_\odot$, and with β_{ST} ranging from -4.5 to

-3.0 . Within this set, and for the polytropic EoS used in Refs. [15,17], some systems undergo spontaneous/induced scalarization, while others dynamically scalarize. As already mentioned, we refer to signals from systems whose components undergo spontaneous/induced scalarization as “spontaneously scalarized signals.” We do so because a necessary condition for induced scalarization to happen is the presence of at least one spontaneously scalarized star. The term “dynamically scalarized signals” will denote those from dynamically scalarized binaries. The strength and type of scalarization that occurs depend sensitively on the constituent masses and the value of β_{ST} .

We now wish to calculate the effective cycles \mathcal{N}_e induced by the ST corrections to investigate their detectability. For the spontaneously scalarized cases, we can compute \mathcal{N}_e with the SPA waveforms, using for $\Delta\Psi(f)$ the terms in square brackets of Eq. (46). The integrated SPA dephasing is then minimized over $(\Delta t, \Delta\phi)$, as explained in Eq. (54). For the dynamically scalarized cases, we compute \mathcal{N}_e with the Fourier transform of the numerical time-domain data of Ref. [17], using for $\Delta\Psi(f)$ the difference in the Fourier phases of a GR and a ST numerical signal. We then again introduce parameters $(\Delta t, \Delta\phi)$ and minimize the integrated dephasing with respect to them to define \mathcal{N}_e , as explained in Eq. (54).

The left panel of Fig. 8 shows the effective cycles as a function of β_{ST} for both spontaneously and dynamically scalarized cases, with the latter labeled with an upside-down triangle. Different line styles correspond to systems with different masses. The shaded region corresponds to the region where one would expect BFs of between 1 and 10, given the results of Fig. 5. Modifications that lead to effective cycles above this shaded region may then be detectable with an aLIGO instrument.

Several features of this figure are worth discussing in more detail. First, observe that almost all of the detectable

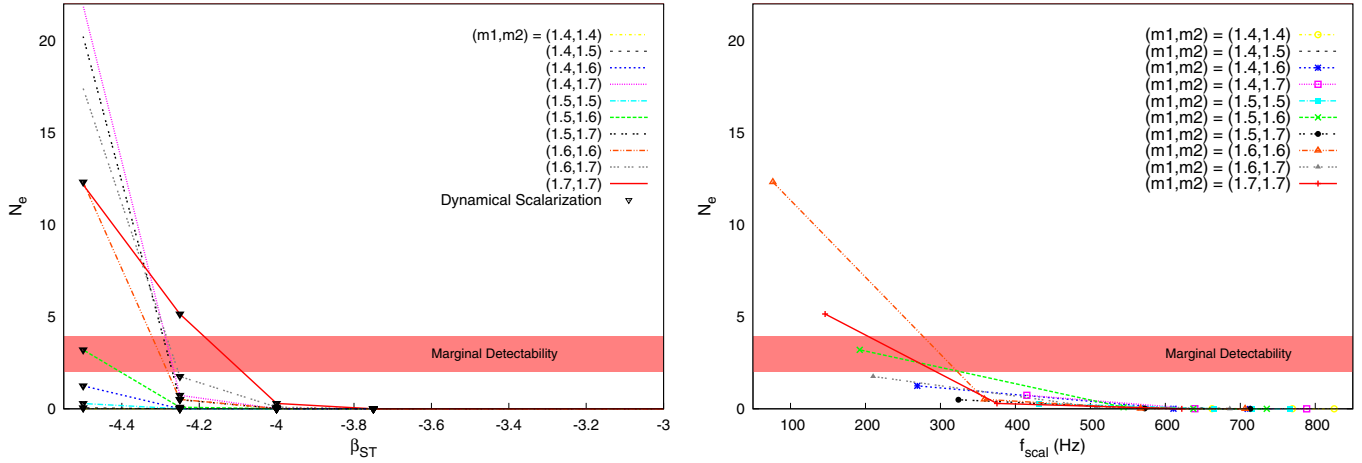


FIG. 8 (color online). Effective number of cycles generated by a ST modification to GW signals as a function of β_{ST} for all ST cases (left) and as a function of GW frequency of scalarization in the dynamical scalarization cases (right). Different curves correspond to systems with different masses, and the different points in the right panel correspond to different values of β_{ST} increasing to the right. We model the GW phase through the SPA in the spontaneously scalarized cases, while we use the Fourier transform of numerical data in the dynamically scalarized cases. The shaded region corresponds roughly to the number of effective cycles necessary for BFs between 1 and 10, as estimated from Fig. 5. Observe that the number of effective cycles is below the detectability region for all but the $\beta_{ST} \lesssim -4.5$ cases. Note also that the only dynamically scalarized cases that are detectable are those in which the scalar field activates at small frequencies. For the equal-mass binaries that undergo spontaneous scalarization, the SPA is not applicable for calculating \mathcal{N}_e . We therefore used masses that were nearly, but not identically, equal for an approximate calculation.

cases correspond to spontaneously scalarized systems. For these systems, dipole radiation is the dominant GR modification, a -1 PN order effect that is proportional to the *difference* of scalar charges of the two bodies [see, e.g., Eq. (46)]. For equal-mass binaries, this dipolar effect vanishes identically, and the dominant modification enters at Newtonian, 0 PN order. Such a GR modification, however, is strongly degenerate with the chirp mass, as shown in Fig. 5, and thus, it is difficult to detect. For this reason, spontaneously scalarized systems with larger mass differences lead to larger values of \mathcal{N}_e and are easier to detect.

Another interesting feature of Fig. 8 is that, within the cases analyzed, only a handful of dynamically scalarized systems seem detectable: the $(m_1, m_2) = (1.6, 1.6)M_\odot$ with $\beta_{ST} = -4.5$ system, the $(m_1, m_2) = (1.7, 1.7)M_\odot$ with $\beta_{ST} = -4.25$ system, and the $(m_1, m_2) = (1.5, 1.6)M_\odot$ with $\beta_{ST} = -4.5$ systems. One of the key differences between these cases and all others is that they scalarize at relatively low GW frequency. Figure 9 shows the approximate GW frequency at which the scalar field activates in a dynamically scalarized binary, as a function of β_{ST} . Observe that as $|\beta_{ST}|$ becomes smaller, or as the total mass of the binary decreases, dynamical scalarization occurs at higher and higher frequencies. For these three cases the scalar field activates at roughly 80, 120, and 180 Hz respectively, while in all other cases dynamical scalarization occurs at higher GW frequency.

The reason, then, that the three dynamically scalarized cases discussed above appear detectable is that detectability

of a *sudden* non-GR effect, i.e., one that turns on rapidly, correlates strongly with the GW frequency at which this turn-on occurs. The right panel of Fig. 8 shows this correlation through \mathcal{N}_e as a function of the GW frequency of dynamical scalarization. Notice that the lower the GW frequency of activation, the larger the number of effective cycles, and thus, the easier it would be to detect such a GR modification.

Reference [22] first observed this phenomenon by studying ppE-type GR modifications that turn on suddenly.

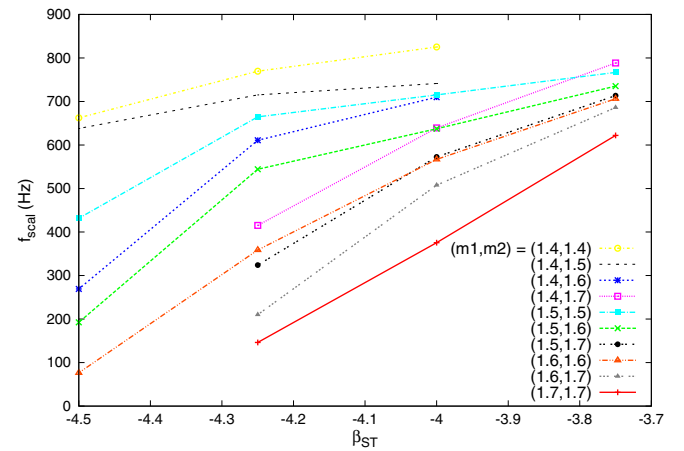


FIG. 9 (color online). Approximate GW frequency in Hz at which the scalar field activates in a dynamically scalarized binary. Observe that the higher β_{ST} and the lower the total mass of the system, the higher the frequency of activation.

Their conclusion was that for aLIGO to detect such non-GR effects at SNRs of 12, the modification had to turn on at a GW frequency lower than roughly 100 Hz (see Fig. 4 in [22]). The ST modifications we study here are of a different PN order and at higher SNR than the non-GR ppE signals considered in Ref. [22], but we still see similar behavior: dynamical scalarization is only detectable when it activates below ≈ 200 Hz at SNR 15.

Summing up, if one detected a GW signal that is consistent with GR (i.e., lacking any dynamical, induced, or spontaneous scalarization effects), one should be able to constrain $\beta_{\text{ST}} \lesssim -4.25$, given the data that we studied in this paper. This statement, of course, is EoS dependent, and thus, strictly applicable only to NSs with the polytropic EoS used here. In principle, NS binaries with a different EoS could scalarize at a different GW frequency. With some variability depending on the EoS, though, it remains true that one must have $\beta_{\text{ST}} \lesssim -4.25$ in order for scalarization (either spontaneous/induced or dynamical) to occur at all.

V. DETECTABILITY OF SCALAR-TENSOR DEVIATIONS: BAYESIAN MODEL SELECTION

In this section, we carry out the second part of our data analysis investigation to determine the detectability of ST deviations in GWs emitted during the inspiral of NS binaries. We perform a full Bayesian analysis study, separating the spontaneously scalarized cases from the dynamically scalarized ones. Such a study will allow us to confirm the expectations derived using effective cycles in the previous section.

To test these expectations, we inject ST GW signals at a SNR ≈ 15 produced by

- (a) *spontaneously scalarized NS binaries*, with spontaneous/induced scalarization occurring *before* GWs enter the detector’s sensitivity band and
- (b) *dynamically scalarized NS binaries*, with dynamical scalarization occurring *during* the inspiral, at GW frequencies in the detector’s sensitivity band.

As a case study for spontaneously scalarized injections, we consider a $(1.4074, 1.7415)M_{\odot}$ binary with $\beta_{\text{ST}} \geq -4.25$. We expect these signals to lead to the largest spontaneous scalarization effects, as one can see in the left panel of Fig. 8 at $\beta_{\text{ST}} = -4.5$. However, for $\beta_{\text{ST}} > -4.25$, we do not expect these effects to be detectable, since they lead to a very small number of effective cycles. Note that for $\beta_{\text{ST}} \rightarrow -4.25$, this system is a case that exhibits dynamical scalarization.

For dynamically scalarized injections, we consider several different systems. First, we study a $(1.4074, 1.7415)M_{\odot}$ binary at $\beta_{\text{ST}} = -4.25$, since this is the limiting case of the spontaneously scalarized sequence discussed in the previous paragraph. We then study a $(1.6441, 1.6441)M_{\odot}$ binary at $\beta_{\text{ST}} = -4.5$, a $(1.7415, 1.7415)M_{\odot}$ binary at $\beta_{\text{ST}} = -4.25$, and a

$(1.5145, 1.6441)M_{\odot}$ binary at $\beta_{\text{ST}} = -4.5$, as these are the dynamically scalarized signals that look the most detectable, given the left panel of Fig. 8.

Spontaneously and dynamically scalarized injections are modeled differently. For the former, we use the SPA scheme of Eq. (46). For the latter, we first compute the discrete Fourier transform of the numerical data of Ref. [17]. We then take the difference of the Fourier phase between a numerical ST signal and a GR signal, and finally add this phase difference to a GR SPA signal.

We recover these injections with four different types of template families:

- (i) *simple ppE templates*, constructed with a single β_{ppE} parameter and ppE exponent $b = -7$,
- (ii) *ST SPA templates*, constructed from the results presented in Sec. III D,
- (iii) *2-parameter ppE templates*, an augmented ppE template family that uses two ppE terms, one with exponent $b = -7$ and one with $b = -6$ [29], and
- (iv) *ppE_θ templates*, another augmented ppE template family with a single ppE exponent $b = -7$ but with $\beta_{\text{ST}} \rightarrow \Theta(f - f^*)\beta_{\text{ppE}}$, where $\Theta(\cdot)$ is a step function and the threshold frequency, f^* , is a new ppE parameter [29].

The simple ppE template family fixes the ppE exponent to $b = -7$, as this corresponds to the leading-order ST correction to the SPA phase for unequal-mass systems where dipolar radiation is present. The ST SPA templates, of course, are the same templates as the model used for the spontaneously scalarized injections, and thus, by construction, we expect these to be the best templates for extracting ST modifications of this type. The 2-parameter ppE template family is also able to achieve a perfect match with spontaneously scalarized injected signals, but it includes two free parameters, rather than one. The ppE_θ template family allows the non-GR terms in the phase to “turn on” at a particular threshold frequency, which is well suited to dynamically scalarized injections.

A salient feature of the semianalytical results of Ref. [17] (and of the full general-relativistic simulations of Ref. [15]) is the binary’s early plunge due to the activation of dynamical scalarization. Such a feature is present in the dynamically scalarized injections we consider, but given the limited number of data sets, we cannot study its detectability in sufficient detail. In order to study whether such rapid termination of the inspiral is detectable, we will consider an additional type of injection and template:

(v) *heaviside signal* of the form $\tilde{h}_{\text{GR}}(f)\Theta(f^* - f)$, where we will vary f^* within $(40, 10^3)$ Hz. Given such injections and templates, we then study the range of f^* that leads to early terminations that can be detected as a non-GR effect. We will explain in Sec. V B why we choose to work with such a toy model.

All the template models considered above are nested. This means that for a certain choice of non-GR parameters,

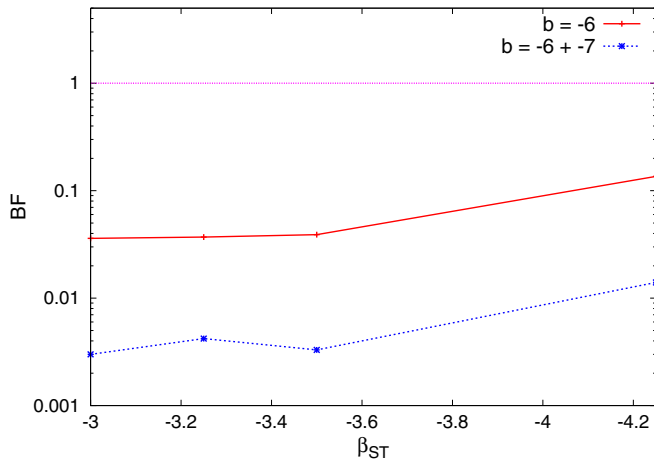


FIG. 10 (color online). The BF in favor of a non-GR signal, calculated by injecting ST signals with SNR of 15, and recovering using both simple ppE templates, and 2-parameter ppE templates. A BF above 1 indicates the data prefer the non-GR model. As expected, neither template is able to detect the non-GR deviations.

the templates reduce exactly to GR. For example, when $\beta_{\text{ST}} = 0$, the ST SPA templates reduce exactly to the GR SPA templates. When this is the case, one can use the Savage-Dickey density ratio to calculate the BF [59]. Finding this ratio requires the calculation of the posterior at the nested value of the non-GR parameter. The posterior is calculated with MCMC techniques well developed in previous studies [22,29,57,60]. We again use the zero-detuned, high-power aLIGO noise curve, assuming a single detector and truncating all integrals at $f = 1000$ Hz.

A. Spontaneously scalarized signals

We first consider spontaneously scalarized signals and compute the BFs between GR and the first two types of

templates described above [(i) and (ii)]. Figure 10 shows the BFs as a function of the injected β_{ST} , keeping $(m_1, m_2) = (1.4074, 1.7415)M_{\odot}$ fixed and varying β_{ST} with the constraint $\beta_{\text{ST}} \geq -4.25$, so as to consider only spontaneously scalarized signals. Because there are no BFs larger than one, this figure shows that spontaneously scalarized ST deviations from GR are not detectable for any of the cases shown. This is consistent with our expectations from the previous subsection. The BFs for the 2-parameter ppE templates are lower than those shown in Fig. 10 for the simple ppE templates because of the Occam penalty for more complicated models, which we will discuss later on in this subsection.

The BF for the spontaneously scalarized, $\beta_{\text{ST}} = -4.5$ case is not included in Fig. 10 because there is so little posterior weight at $\beta_{\text{ppE}} = 0$ that a calculation of the BF using the Savage-Dickey density ratio is poorly defined. That is, the Savage-Dickey density essentially diverges due to poor exploration of the $\beta_{\text{ppE}} = 0$ region. Figure 11 shows the posterior distribution for β_{ppE} , which illustrates this point and, as expected, indicates that the spontaneously scalarized binary with $\beta_{\text{ST}} = -4.5$ is easily detectable, for the polytropic EoS models considered here.

One may worry that our inability to detect spontaneously scalarized binaries when $\beta \geq -4.25$ is somehow a consequence of using ppE templates. To prove that this is not the case, we next explore the extraction of such spontaneously scalarized signals using both ppE_{θ} and custom-made, SPA templates. The ppE_{θ} templates should have more freedom to fit these signals, and the SPA templates can fit them perfectly. Because of the nature of these waveforms and the weakness of the GR deviation in the injections, the non-GR parameters in both cases are essentially unconstrained within their prior ranges. For the SPA templates, the non-GR parameter is β_{ST} , and its prior range is $|\beta_{\text{ST}}| < 5$. This means that the BF is approximately equal

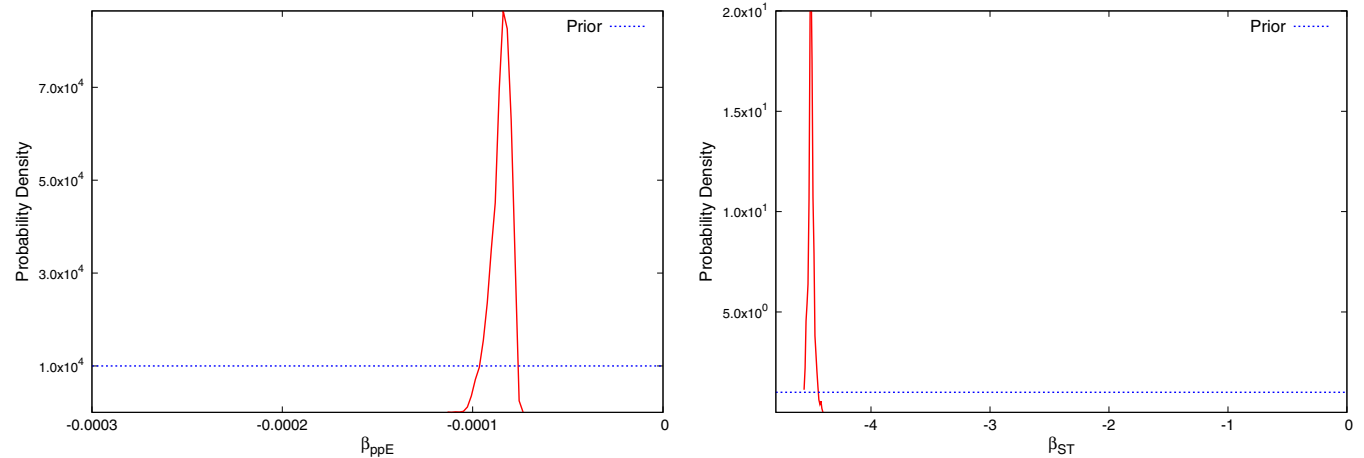


FIG. 11 (color online). Red (solid) lines: the posterior distributions for β_{ppE} (left panel) and β_{ST} (right panel). Blue (dashed) lines: the prior density for each of these parameters. There is essentially zero posterior weight at $\beta_{\text{ST/ppE}} = 0$, indicating a large preference for the non-GR model from both template families.

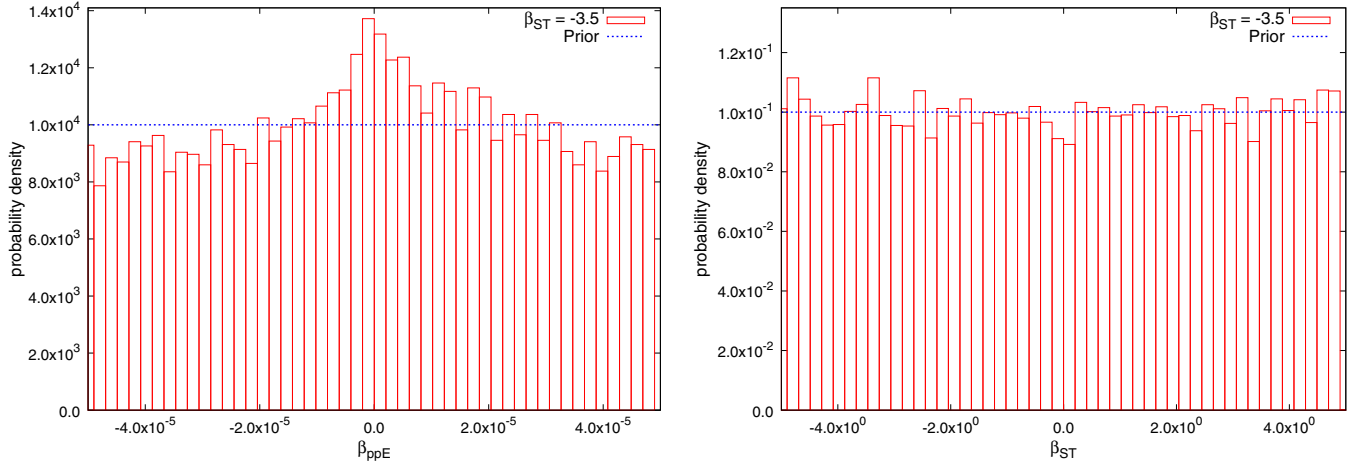


FIG. 12 (color online). Posterior distributions for β_{ST} (right) and for β_{ppE} (left), recovered from a SNR 15 injection with $\beta_{ST} = -3.5$. Also plotted in blue (dashed) lines is the prior density for both parameters. The parameters are essentially unconstrained within their prior range, leading to a BF ≈ 1 for both models, indicating no preference between this model and GR.

to one in both cases, independent of the injected parameters. Figure 12 shows the prior and posterior distributions generated using the ppE $_{\theta}$ and the SPA templates, for a spontaneously scalarized binary with $\beta_{ST} = -3.5$. These distributions are identical for other injected values of β_{ST} , barring $\beta_{ST} \leq -4.5$, which is again easily extractable as a non-GR signal with either type of template.

We expect, though, that custom-made templates should perform better than ppE templates at extracting non-GR modifications when the custom-made templates match the signal. The extent to which this is true depends on the strength of the non-GR modification and on the loudness of the signal. Let us first consider very strong ST modifications, which we have already shown to be detectable with simple ppE templates, i.e., a $\beta_{ST} = -4.5$, spontaneously scalarized ST signal, with masses of $(1.4074, 1.7415)M_{\odot}$ and SNRs of 12, 10, 8, and 6. When the SNR is 12, 10, or 8, there is *no* difference in the ability of simple ppE or SPA templates to discern the presence of a ST effect. When the SNR drops below 8, the signal is not detectable in the first place, using either type of template. Thus, custom-made templates and model-independent templates are equally good at detecting this type of GR deviations.

But what about GR deviations that are weaker, and thus, more difficult to detect? Surely, in this case one expects custom-made templates to be more effective at discerning such deviations. To explore this question, we inject a $\beta_{ST} = -3.5$, spontaneously scalarized ST signal, with masses $(1.4074, 1.7415)M_{\odot}$ and *very* high SNRs (so that the non-GR modifications are detectable). We then recover these signals using both the SPA templates and the simple ppE templates. For the former, we again use the prior range on β_{ST} of $|\beta_{ST}| \leq 5$, while for the latter the prior range on β_{ppE} is a bit trickier. We could use the same prior range on β_{ppE} as in the previous subsection, but this was motivated from a study of signals at SNR ≈ 20 . The bounds on β_{ppE}

for the extremely high SNR signals we are studying in this subsection should be much stronger. We estimate the latter by relating the -1 PN coefficient from our SPA waveform to the ppE strength parameter when $b = -7$. This leads to a prior range on β_{ppE} of $|\beta_{ppE}| \leq 1.035 \times 10^{-10}$. We then calculate the BF for the simple ppE model using both the full and the more restricted prior range on β_{ppE} .

Figure 13 shows the BF as a function of the SNR between GR and either the SPA or the simple ppE templates, using both prior ranges for the ppE templates. Notice that the SPA templates detect the modifications at a much lower SNR than the ppE templates using the full prior, and at an SNR approximately half the value necessary for the ppE templates with the restricted prior. Low SNR,

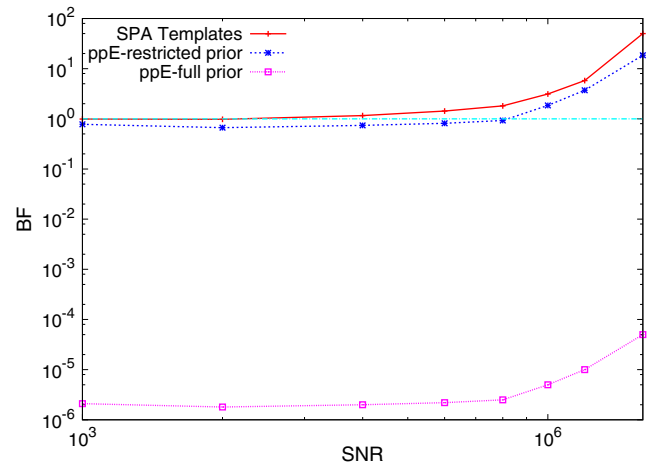


FIG. 13 (color online). BFs in favor of modified gravity as a function of SNR, calculated by injecting a signal with $\beta_{ST} = -3.5$. A BF over 1 indicates a preference for a non-GR theory of gravity. The red (solid) line shows the BFs calculated using SPA templates, and the blue (dashed) line shows those calculated from ppE templates.

however, is a relative term. The SPA templates detect the GR modifications at SNRs $\approx 6 \times 10^5$, which corresponds to a ridiculous luminosity distance of $\approx 10^3$ pc (essentially inside the Milky Way).

Although we expected that the custom-made SPA templates would be more effective than the generic, ppE templates at extracting signals (at sufficiently high SNR), it is still worth studying the reason behind this expected result. To do so, we examine the prior and posterior distributions of the two non-GR parameters, β_{ST} and β_{ppE} , and the *Occam penalty* that arises from each parameter. The Occam penalty is a built-in feature of Bayesian analysis, which causes simple models to be favored over more complicated ones. That is, models with fewer parameters are preferred to models with extra parameters, all else being fixed.²

This brings us to an explanation of the results in Fig. 13. Figure 14 shows the posterior distributions for β_{ST} and β_{ppE} , using both the full and the restricted priors, for a signal with SNR of 6×10^5 , plotted over the entire prior range. The prior distribution is plotted in all three cases, although it is only visible for β_{ST} and for β_{ppE} with the restricted prior range. Notice that, where the posteriors for β_{ST} and β_{ppE} in the restricted case have some weight over most of their entire prior ranges, β_{ppE} for the full prior range is hugely constrained—so constrained that its posterior distribution looks like a delta function. This means that there is a very large Occam penalty disfavoring this model, and it will take a signal of extremely high SNR to overcome this penalty. As seen from the results in this section, a tighter prior range leads to a smaller Occam penalty, and thus a larger BF in favor of the GR deviation.

B. Dynamically scalarized signals

Section IV C hinted that dynamical scalarization is much more difficult to detect than spontaneous scalarization. In fact, Fig. 8 shows that the number of effective cycles accrued in dynamically scalarized signals is rather low in general. An example of this is the dynamically scalarized, $\beta_{\text{ST}} = -4.25$ case for a binary with masses $(1.4074, 1.7415)M_{\odot}$. Indeed, a Bayesian analysis of this signal shows that such a ST effect is not detectable with simple ppE or 2-parameter ppE templates.

One way to understand this is by considering the amount of SNR that is accrued in the signal after scalarization has set in. Table I lists the percentage of the total SNR² contained in the signal *before* at least one of the NSs

²Consider two nested models: \mathcal{M}_1 which is parametrized by a single parameter, θ , and \mathcal{M}_0 which is unparametrized, i.e., has $\theta = \theta_0$ where θ_0 is a constant. If the likelihood function for \mathcal{M}_1 is a Gaussian, then $\text{BF}_{1,0} \propto (\delta\theta)/\Delta\theta$, where $\delta\theta$ is the characteristic width of the posterior in θ , and $\Delta\theta$ is the prior range of θ [60]. Thus, if the value of θ is entirely unconstrained by the data, there is no penalty for an extra parameter. On the other hand, if θ is very tightly constrained, there is a large penalty.

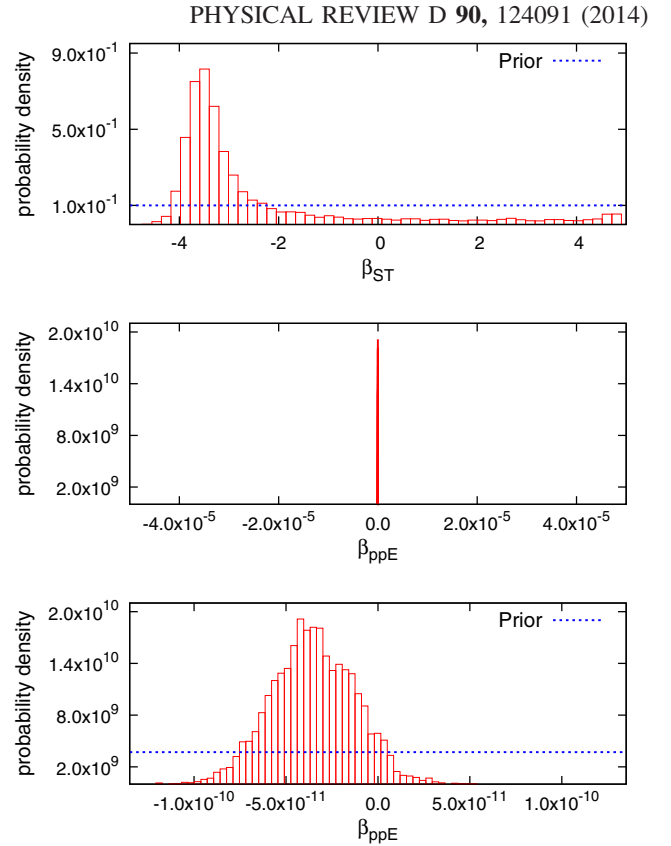


FIG. 14 (color online). Posterior distributions for β_{ST} (top panel) and β_{ppE} with the full prior (middle panel) and restricted prior (bottom panel), generated by recovering a SNR 600000 signal with $\beta_{\text{ppE}} = -3.5$. Also plotted are the prior densities, although this is not visible in the middle panel. The posterior for β_{ppE} is so highly constrained compared to the full prior that it is nearly impossible to use this model for the detection of a ST modification to gravity.

has become scalarized, for signals with $\beta_{\text{ST}} = -4.25$. The frequency at which either NS becomes scalarized can be easily extracted by looking at the behavior of the scalar charges as a function of orbital frequency (see Fig. 9). From this table, it is clear that there is very little SNR accumulated over the portion of the signal in which scalarization effects are important. Moreover, this SNR accumulation

TABLE I. The percentage SNR squared accrued before dynamical scalarization has begun, for signals with $\beta_{\text{ST}} = -4.25$ and SNR ≈ 15 . The first column gives the mass of the system, the second the approximate frequency at which dynamical scalarization begins, and the third the percentage of the SNR² accumulated prior to scalarization. Note that for all cases most of the SNR² of the signal is amassed before scalarization becomes significant.

Mass	Frequency [Hz]	%SNR ²
$(1.4074, 1.7415)M_{\odot}$	314	98.1
$(1.5145, 1.7415)M_{\odot}$	301	94.25
$(1.6441, 1.7415)M_{\odot}$	286	89.6

TABLE II. Luminosity distance to the source such that the SNR recovered (up to a threshold frequency f_{inj}^*) is equal to 8. The third row shows the total SNR that would be recovered at the given luminosity distances if $f_{\text{inj}}^* = 1000$ Hz. Note how rapidly the distance to the source has to be decreased as the threshold frequency is decreased.

f_{inj}^* [Hz]	100	65	51	44	39
D_L [Mpc]	60	30	18	12	9
SNR	15	30	50	75	100

does not occur in the frequency region in which the instrument is most sensitive.

The reason why the $\beta_{\text{ST}} = -4.25$, dynamically scalarized case cannot be easily detected is precisely that the frequency at which ST modifications become noticeable is rather large. But this frequency is, of course, a function of the masses of the binary and the EoS used. Recall that dynamical scalarization sets in when the energy of the system, roughly speaking the linear combination of the NS compactnesses and the (absolute value of the) gravitational binding energy, exceeds a certain threshold. Therefore, one can imagine a NS binary whose masses and radii are such that the NS compactnesses are very close to exceeding the energy threshold, and thus, dynamical scalarization can set in at very low frequencies, as shown in Fig. 9.

From the effective cycle study illustrated in Fig. 8, it appears that the dynamically scalarized binaries that are most easy to detect are those described at the beginning of Sec. V: a $(1.6441, 1.6441)M_{\odot}$ binary at $\beta_{\text{ST}} = -4.5$, a $(1.7415, 1.7415)M_{\odot}$ binary at $\beta_{\text{ST}} = -4.25$, and a $(1.5145, 1.6441)M_{\odot}$ binary at $\beta_{\text{ST}} = -4.5$. Let us first consider a signal described by the first of these sets of parameters and extract it with a simple ppE template. Such a signal dynamically scalarizes at the lowest frequency of all systems considered (at roughly 80 Hz). This system is indeed detectable, leading to a very large BF and a β_{ppE} posterior that is similar to that shown in the left panel of Fig. 11 for a spontaneously scalarized, $\beta_{\text{ST}} = -4.5$ binary with masses $(1.4074, 1.7415)M_{\odot}$. The width of the β_{ppE} posterior, however, is roughly one order of magnitude larger than in the spontaneously scalarized case, with a variance of $\sigma_{1.6,1.6} = 3.7 \times 10^{-5}$ for the former and $\sigma_{1.4,1.7} = 5 \times 10^{-6}$ for the latter, indicating that the BF in this case is smaller, as expected.

We can now repeat this analysis for the other two binaries that we expect may be detectable given Fig. 8. For both cases, we find that $\text{BF} \approx 3$, obtained from the Savage-Dickey ratio. This is again in accordance with expectations from Fig. 8. For the $\beta_{\text{ST}} = -4.25$ system, the number of effective cycles indicates a marginal detection, which is precisely what we find in this Bayesian analysis. For the $\beta_{\text{ST}} = -4.5$ system, the number of effective cycles plotted in Fig. 8 suggests the possibility of detection; however, recall that the numbers shown in this figure are

upper limits. In this case, our Bayesian analysis indicates that this upper limit is higher (by a factor of ≈ 2) than the actual number of effective cycles induced by dynamical scalarization of the binary components.

As already mentioned, our analysis thus far has not focused on one important feature of dynamically scalarized signals: the early plunge of the NS binary. That is, once the GW frequency has exceeded the threshold for dynamical scalarization to set in, the NS binary inspirals for a few more cycles, but then plunges and merges soon after. This occurs much earlier than in GR (see, e.g., Figs. 10 and 15 in [17]). Of course, after the NSs have merged, either a hypermassive NS forms, with a rotating bar that emits GWs at kHz frequencies, or a BH forms, thus cutting out GW emission exponentially through ringdown. The precise form of the waveform during this merger and ringdown phase will depend strongly on the NS equation of state.

We study in an *approximate* fashion whether an early plunge can be detected in a generic modified gravity theory by considering a set of Heaviside signal injections, i.e., GR waveforms for which the Fourier amplitude is multiplied by a Heaviside function with argument $f_{\text{inj}}^* - f$, as we vary the injection cutoff frequency $f_{\text{inj}}^* \in (40, 10^3)$ Hz. In dynamically scalarized systems, however, the transition from inspiral to early plunge and then merger is *smooth*, while Heaviside templates are clearly not. Therefore, it is obvious that the latter are inappropriate templates to extract realistic dynamical scalarization signals. However, they are good and simple toy models to study whether an early plunge (and thus an early termination) of the signal could be detected as a non-GR effect in data analysis. Since a smooth transition will be less noticeable than a sharp Heaviside transition, the use of Heaviside templates could be thought of as conservative; i.e., if a GR deviation cannot be observed with such an abrupt termination, it certainly will not be detectable if the transition is smooth.

We carry out such a study in the following way. We place all such systems at $D_L = 30.75$ Mpc such that the recovered SNR is approximately 15 when $f_{\text{inj}}^* = 100$ Hz and 30 when $f_{\text{inj}}^* = 1000$ Hz. For that value of f_{inj}^* , the Heaviside signal is thus similar to those we have been analyzing throughout this paper and also those studied in Ref. [29]. We then extract such injections with templates that exactly match the signal, but with f^* included as a template parameter to search over, as well as with simple ppE templates with $b = -4$. This value of the exponent parameter is chosen because of its strong correlation with the total mass, which is the parameter that determines the cutoff frequency in GR. As explored in Ref. [22], the specific value of b that is chosen has little impact on the analysis.

One may worry that approximating the early plunge in this abrupt way may mask the detectability of non-GR effects, as the cycles that are effectively thrown out by this sort of study would contain these effects. Because there is

TABLE III. Luminosity distance to the source such that the SNR recovered (up to a threshold frequency f_{inj}^*) is equal to 8. The third row shows the total SNR that would be recovered at the given luminosity distances if $f_{\text{inj}}^* = 1000$ Hz. Note how rapidly the distance to the source has to be decreased as the threshold frequency is decreased.

f_{inj}^* [Hz]	100	65	51	44	39
D_L [Mpc]	60	30	18	12	9
SNR	15	30	50	75	100

so little SNR contained in those final few cycles of inspiral, however, this should not be an issue. For the systems studied in this paper, there are thousands of orbital cycles before scalarization is activated, and only tens of orbital cycles afterwards. Additionally, for all but a few cases, the orbital cycles that are affected by scalarization occur at a frequency in which the detectors are not very sensitive. These two effects combined mean that there is very little information being discarded by abruptly terminating the waveforms once scalarization has occurred.

Clearly, the earlier the binary plunges (or, in our case, the lower the injection cutoff frequency, f_{inj}^*), the fewer GW cycles the signal will contain in the sensitivity band of the detector. This then translates to a smaller recovered SNR. Thus, in order to detect such a signal at all, we must either be fortunate enough to detect systems that are sufficiently nearby, or fortunate enough to detect enough events such that their stacked SNR is large. Table II shows the luminosity distance required such that the SNR recovered equals 8 for different termination frequencies f_{inj}^* . This table also shows what the SNR would have been at such luminosity distances, if the signal did not terminate at f_{inj}^* , but rather continued to 1000 Hz.

Figure 15 shows the posterior distributions for the recovered values of f^* using Heaviside templates, and the posteriors for the recovered values of β_{ppE} using simple ppE templates. All injections focus on a $(1.6, 1.6)M_{\odot}$ NS binary, with the same polarization angle and sky position as all other injections in this paper, and $D_L = 30.75$ Mpc. The prior range on the search parameter f^* is uniform between 0 to 1000 Hz for the Heaviside templates, and

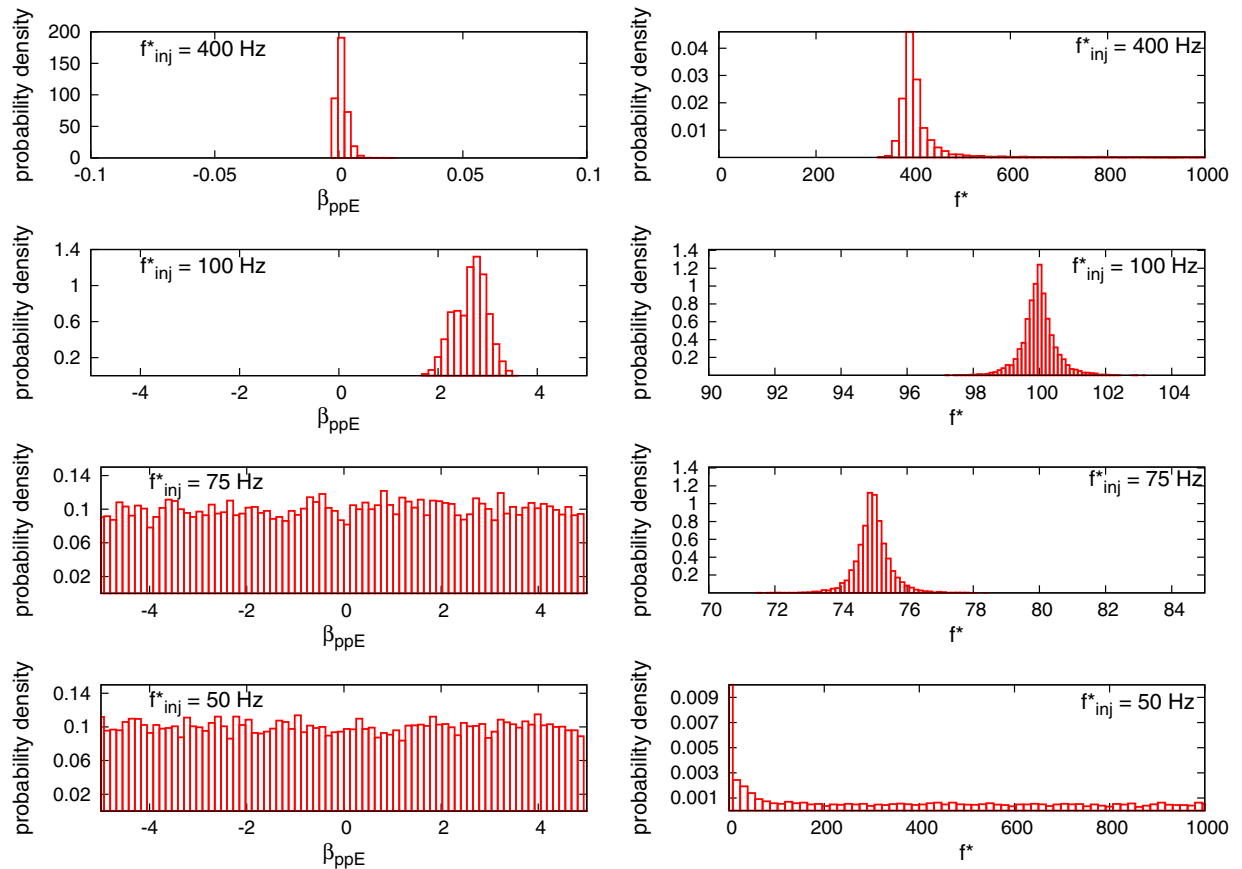


FIG. 15 (color online). Left panels: posterior distributions for β_{ppE} , recovered by extracting a Heaviside template injection with injected cutoff frequency f_{inj}^* , using simple ppE templates. The only case that shows a strong preference for the non-GR model is for $f_{\text{inj}}^* = 100$ Hz. Right panels: posterior distributions for the recovered f^* , generated by extracting a Heaviside injection with templates of the same family and different injected cutoff frequencies f_{inj}^* . Here, the cases with $f_{\text{inj}}^* = 100$ Hz and $f_{\text{inj}}^* = 75$ Hz are distinguishable from GR.

thus, the prior density is $1/1000 = 0.001$. Recall that the prior range on the search parameter β_{ppE} is also uniform with range -5 to 5 for the simple ppE templates, and thus, the prior density is $1/10 = 0.1$ in this case.

The interpretation of the posterior distributions for the recovered values of f^* as tests of GR is somewhat subtle, because it is not entirely clear what the ‘‘GR value’’ for f^* should be. In principle, the inspiral should end when the NSs begin to plunge, and certainly by the time the stars have come into contact. The GW frequency of the latter, f_{cont} , depends both on the component masses and the EoS; for a $(1.6, 1.6)M_{\odot}$ binary it is between 1250 and 2050 Hz, depending on the NS radius. As a simple and practical measure of the plunge, one could choose the GW frequency at the innermost stable circular orbit (ISCO) of a test particle in a Schwarzschild spacetime: $f_{\text{ISCO}} = 6^{-3/2}/(\pi M)$; for a $(1.6, 1.6)M_{\odot}$ NS binary, $f_{\text{ISCO}} = 1354$ Hz. This is a suitable measure for the beginning frequency of plunge in GR, provided the NS is compact enough such that its contact frequency is above f_{ISCO} . For the systems we study here, $f_{\text{cont}} > f_{\text{ISCO}} > 1000$ Hz, where we recall that the latter is the highest frequency of integration in all cross-correlations. We can therefore take the GR value of f^* to be 1000 Hz, and calculate the BF by comparing posterior and prior densities at this point.

The right panels of Fig. 15 show that the Heaviside templates are able to distinguish a deviation from GR provided the injected cutoff frequency f_{inj}^* is above ≈ 50 Hz and below ≈ 400 Hz. These panels present the posterior distributions for the parameter f^* , recovered using Heaviside templates on injections with various values of f_{inj}^* . The ability of Heaviside templates to distinguish GR deviations can be established by computing the BFs for each of these panels through the Savage-Dickey density ratio (recall that the BF is the ratio of the posterior to the prior density at the GR value of the search parameter, $f^* = 1000$ Hz in the Heaviside template case). For instance, the BF ≈ 1 when $f_{\text{inj}}^* = 50$ Hz, while the BF ≈ 5 when $f_{\text{inj}}^* = 400$ Hz, a marginal detection of a GR deviation.

The left panels of Fig. 15 show that the ppE templates can also distinguish Heaviside-type deviations from GR, but this time provided f_{inj}^* is above ≈ 75 Hz and below ≈ 400 Hz. These panels present the posterior distributions for β_{ppE} , recovered using a simple ppE template with $b = -4$ on Heaviside injections with various values of f_{inj}^* . The BF can still be computed through the Savage-Dickey density ratio, except that now GR is recovered when the value of β_{ppE} is zero, and we recall that the prior density is 0.1. For instance, the BF ≈ 1 when $f_{\text{inj}}^* = 75$ Hz, while the BF is clearly much larger than unity when $f_{\text{inj}}^* = 100$ Hz.

Why is detectability of a GR deviation difficult for very low or very large f_{inj}^* ? For very low injected cutoff frequencies (e.g., below 50 Hz for the Heaviside templates and 75 Hz for the ppE templates), the analysis fails to detect a signal altogether—a reasonable result, considering that

these very low injected cutoff frequencies drop the total recovered SNR of the signal below 8. For very high injected cutoff frequencies (e.g., above 400 Hz), the deviation from GR occurs too far outside of the detector’s most sensitive band to be noticeable. Put another way, not enough SNR is accrued while the GR deviation is active.

Although the choice of a signal at $D_L = 30.75$ Mpc leads to a recovered SNR ≈ 30 when $f_{\text{inj}}^* = 1000$ Hz, a reasonable choice for comparison to other results in this paper, systems at such a close distance are not very likely. A more reasonable expectation is a system at twice that luminosity distance, $D_L \approx 61.5$ Mpc, such that the signal that *would* have total SNR of ~ 15 if $f_{\text{inj}}^* = 1000$ Hz, but which, if subject to the early plunges analyzed here, is in fact a signal with lower recovered SNR. When we inject Heaviside signals at such a D_L , so that the SNR ~ 15 if $f_{\text{inj}}^* = 1000$ Hz, we find results qualitatively similar to those described in the previous paragraph, but with a narrower detectable injected cutoff frequency range. The high injected cutoff frequency for detectability drops to ≈ 300 Hz, and the low cutoff frequency rises to ≈ 90 Hz. This result is in accordance with expectations.

The ability to detect the early plunge of a binary system may have an important implication in terms of the detectability of dynamical scalarization. As we have seen in Fig. 9, higher-mass NS binaries can dynamically scalarize at frequencies below 400 Hz for $\beta_{\text{ST}} \approx -4$. This then suggests that the inclusion of an early plunge, the merger, and the postmerger phase in a data analysis study may allow for constraints on ST theories at such values of β_{ST} . Notice, in particular, that such constraints are stronger than those obtained when including only the inspiral phase.

One must be very careful, however, when extrapolating results and promptly concluding that the inclusion of the plunge and merger portions of these signals will increase their distinguishability. First, there are very few cycles in the postplunge phase, and thus very little SNR accumulated after the plunge. Second, and perhaps more importantly, the postplunge phase will be strongly affected by the NS equation of state. Degeneracies between equation-of-state effects and non-GR effects imply that the postplunge phase of NSs may not be as useful as a means to test GR. Of course, a more detailed analysis is required to derive solid conclusions.

VI. CONCLUSIONS

In this paper, we sought to answer one overarching question: can deviations from GR in GW signals that are caused by a certain class of ST theories be detected with aLIGO-type instruments? We find that this is the case, irrespective of whether the deviation arises from spontaneous/induced or dynamically scalarized NSs. These projected constraints will be complementary and at least comparable to current binary pulsar ones.

Not all spontaneous/induced and dynamical scalarization effects, however, are easily detectable. For a spontaneous/induced scalarization to be detectable, the scalar field anchored on each NS must be large enough, and the masses sufficiently dissimilar, that dipole radiation becomes important. This occurs, for example, for values of $\beta_{\text{ST}} \approx -4.5$ and a NS binary with masses $(1.4, 1.7)M_{\odot}$, for the simple polytropic EoS that we consider in this paper (with a different EoS potentially changing these values). For a dynamically scalarized effect to be detectable in aLIGO, such scalarization must occur at a sufficiently small GW frequency so that enough GW cycles are affected in a frequency region that detectors are sufficiently sensitive to. This occurs, for example, for values of $\beta_{\text{ST}} \approx -4.5$ and a NS binary with masses $(1.6, 1.6)M_{\odot}$, which scalarizes at a GW frequency of roughly 80 Hz (again with some variability of these values depending on the EoS).

We additionally investigated the detectability of another effect associated with dynamical scalarization: the early plunge that would be induced in binaries that undergo such scalarization. We found that the sudden cutoff of a GW signal at frequencies below those expected in signals described by GR is detectable using both simple ppE templates and GR templates with a Heaviside function, for certain ranges of cutoff frequencies. Such a plunge, for example, could occur for values of $\beta_{\text{ST}} = -4$ and a NS binary with masses $(1.7, 1.7)M_{\odot}$. Of course, an early plunge cannot be accurately modeled through a Heaviside function, and so a more careful data analysis study that includes inspiral-merger-postmerger signals is needed.

In the process of reaching these answers, we explored a measure that can help estimate whether different types of phase effects are detectable with GWs: the effective cycles of phase. We found that for a wide variety of different non-GR signals, the modification to the GR phase needs to lead to roughly 4 cycles of effective phase to be detectable with an aLIGO detector at SNR 15. We further found that such detectability is independent of whether one uses custom-made ST templates or model-independent templates to search for deviations at the expected SNRs of aLIGO-type detectors.

A final question that we considered was whether custom-made, theory-specific templates are more useful at detecting deviations from GR than the model-independent ppE template family. We answered this question by looking at both extremely high SNR signals with ST signatures that were undetectable at low SNR, and by looking at low SNR signals with ST signatures that were easily detectable at reasonable SNR. In both cases, we found that ppE templates perform almost as well as custom-made, SPA templates at distinguishing non-GR signals from GR ones.

Future work could concentrate on extensions of the analysis presented here. One interesting extension would be to repeat this work for NSs with realistic EoSs. The work in

Refs. [15,17], which we used in this paper exclusively, used a polytropic EoS, but this is easily generalizable to more realistic EoSs (cf. Ref. [21]). One may find EoSs and masses that do not lead to spontaneous/induced scalarization for binary pulsars, yet lead to spontaneous/induced scalarization for systems that can be detected with GWs. Such systems would thus evade binary pulsar constraints and yet potentially lead to detectable deviations with aLIGO. Again, it is important to emphasize that stiffer/softer EoSs will lead to qualitatively (and quantitatively) different behavior. A very stiff EoS could perhaps support more compact stars that spontaneously scalarize at lower frequencies. A systematic study of these effects is left for future consideration.

Another interesting analysis would be to study whether one can find EoSs or masses for which dynamical scalarization sets in at very low frequency, e.g., close to 10 Hz. Reference [22] estimated that for an abrupt GR modification to be detectable with an aLIGO-like detector at SNR 10, such a modification would have to start at a GW frequency below 100 Hz. Most cases of dynamical scalarization that we explored occur at ~ 200 Hz or higher, but there are some instances in which scalarization occurs at a lower frequency, and it is possible that different mass/EoS combinations would produce more of these scenarios.

Other extensions may include adding more complexity to the signals and the templates, through the inclusion of the merger and postmerger phases, as well as the inclusion of spin [61–64] and eccentricity [43] effects. Recall that with respect to second-generation, ground-based detectors it is common to regard the NS merger and postmerger phases as unimportant for testing GR as they occur at kHz frequencies where such detectors are least sensitive. Dynamically scalarized NSs, however, could plunge at much lower frequencies, and such effects may be detectable. References [63,64] showed that the inclusion of spin in NS binaries can have a large effect on parameter estimation. Similar conclusions were arrived at when including more complexity in GW signals to test GR (see, e.g., [65–67]). Also, Ref. [17] showed that eccentric NS binaries in ST theories can give rise to scalarization/descalarization phenomena that may affect the binary’s orbital evolution (effectively decreasing the eccentricity faster than in GR) at sufficiently low frequencies to be detected.

Another interesting avenue for future work would be to repeat the analysis of this paper but with a non-template-based search algorithm that may be more sensitive to the postmerger phase. In our analysis, we used a template-based search of inspiral signals, neglecting the postmerger phase that occurs at high GW frequencies where aLIGO’s sensitivity will be weaker. Recently, however, Ref. [68] used a template-free burst algorithm to show that the merger phase may be sufficiently detectable by aLIGO to discern between a prompt collapse scenario and the formation of a hypermassive NS, if the event occurs at

≈ 10 Mpc. Dynamical scalarization will modify the post-merger phase, also leading to either prompt collapse or hypermassive NS formation, depending on the masses of the binaries. Such effects, however, will probably be somewhat degenerate with the EoS, and thus, it is unclear whether merger modifications will be strong enough to detect a GR deviation.

One final way to study the robustness of our conclusions would be to consider GW detection with a network of GW detectors, with second-generation detectors and noise tuning, with a large number of second-generation detections and stacking [69,70], or with future GW detectors, such as the Einstein Telescope [71]. All of these could lead to much lower noise at GW frequencies around 100 Hz, which would then have multiple effects. First, better sensitivity at 100 Hz should push the threshold frequency at which GR deviations can be detected to higher frequencies. Second, better sensitivity overall should lead to individual detections with higher SNR and to a higher number of detections per year. Combining all of this, and perhaps through the use of stacking, one may be able to detect dynamical scalarization for lower values of $|\beta_{\text{ST}}|$. One should keep in mind, however, that the direct detection of the additional breathing mode will be extremely hard, even when detecting GWs with multiple instruments, since in ST theories that pass Solar System tests, the interaction of such modes with a detector is suppressed by ψ_0 [15], which is constrained to $\lesssim 10^{-2}$ because of the Cassini bound.

Finally, let us address the relationship between our work and that reported in Ref. [72], which appeared after the submission of this paper. One may be led to believe that the conclusion arrived at in this paper and those of Ref. [72] are not in agreement, with respect to the detectability of scalarization effects with aLIGO. Reference [72] first calculates the total number of cycles of phase that are accumulated in a GW signal due to the presence of scalarization effects. They then note that this number is larger than or comparable to the total number of cycles of phase that will be accumulated due to EoS effects within GR. Since the latter may be detectable with next generation detectors [70,73,74], they then argue that scalarization effects may also be detectable. This conclusion is in fact in *agreement* with our findings because EoS effects can be measured only provided the SNR is sufficiently high (roughly above 30). Our analysis used SNRs in the tens, as expected from the first few years of detection; for such signals, non-GR effects are not detectable. Reference [72] also finds that scalarization can be detected when it occurs at GW frequencies larger than roughly 130 Hz, which is in perfect agreement with our findings (once one converts orbital to GW frequency).

Although Ref. [72] does not claim that the total cycles of phase due to a particular effect can directly tell us about detectability, it is possible to misread the conclusions of this

paper to indicate that they can. We therefore emphasize again here that the total cycles of phase have no analytic connection to the Bayes factor and, in fact, fail to account for parameter covariances. This affects detectability in two main ways. One is obvious—a non-GR phase term that has large correlations with other system parameters will be easy to fit using GR templates. This will make the effect very difficult to discern, as illustrated in Fig. 5. The other, less obvious consequence is that although effects that enter at high PN order accumulate more slowly, they may be detectable when they lead to smaller numbers of phase cycles than those that enter at low PN order. This is again directly due to parameter covariances. In the case of spontaneous or dynamical scalarization, non-GR effects that enter at low PN order will have high covariances with system parameters, such as the chirp mass. Higher PN order effects will have weaker covariances, but they lead to much weaker effects, with most of the total dephasing accumulating from the low PN order terms that have large covariances. Thus, the use of total cycles of phase to claim detectability of non-GR effects is not appropriate and one should really either use the effective cycles discussed in this paper or a full Bayesian analysis.

Also, Ref. [72] (at least in its first arXiv version) states that the simulations of Ref. [15] “misread” the output of the LORENE code used to determine the simulation initial data, and claims that the gravitational masses given in Ref. [15] are incorrect. This is certainly not the case and the gravitational masses we give in Ref. [15] are exactly those of the LORENE output. As it is well known, there is no unambiguous way of defining individual gravitational masses for a tight binary system within general relativity. We provided the readers of Ref. [15] with the exact LORENE-given gravitational masses in order to clearly identify our initial data and ensure our results will be reproducible by others. An alternative, which is the one followed in Ref. [72], would have been to give the gravitational masses of the stars in isolation, but this may have caused unnecessary confusion, as the gravitational masses are never used in Ref. [15] except for identifying the initial data.

Reference [72] also raises question on the dynamics of the most massive case presented in Ref. [15] and used here. Their concern is related to our choice of initial data for such an already scalarized case, and is about whether this could cause an earlier plunge. Such a concern was already addressed in Ref. [17], where we (i) show the results of simulations with large initial separations (e.g., Figs. 4 and 5, where no plunge is present at large separations) and (ii) validate our simulations with an enhanced PN model. Moreover, we stress here that the initial data used in Ref. [15] for the low-mass case with dynamical scalarization are exact (because in the absence of spontaneous scalarization, the ST initial data are the same as in GR).

ACKNOWLEDGMENTS

We thank Gilles Esposito-Farese and Gabriela Gonzalez for insightful conversations. N. Y. acknowledges support from NSF Grant No. PHY-1114374 and the NSF CAREER Award No. PHY-1250636, as well as support provided by the National Aeronautics and Space Administration from Grant No. NNX11AI49G, under Sub-award No. 00001944. L. S. and N. J. C. acknowledge support from NSF Grant No. PHY-1306702. E. B. acknowledges support from the European Union's Seventh Framework Programme (FP7/PEOPLE-2011-CIG) through the Marie Curie Career Integration Grant GALFORMBHS PCIG11-GA-2012-321608. A. K. is supported by NSF CAREER Grant No. PHY-1055103. L. L. acknowledges support by NSERC through a Discovery Grant and CIFAR. L. L. thanks the Institut d'Astrophysique de Paris and the ILP LABEX (ANR-10-LABX-63), for hospitality during a visit supported through the Investissements d'Avenir Programme under Reference No. ANR-11-IDEX-0004-02. Research at Perimeter Institute is supported through Industry Canada and by the Province of Ontario through the Ministry of Research and Innovation.

APPENDIX A: SCALAR-TENSOR THEORIES WITH $\beta_{ST} < 0$

In this Appendix, we discuss how ST theories with $\beta_{ST} < 0$ repel cosmological solutions away from their GR counterparts. This will be done by essentially repeating the analysis in Refs. [18,19] (see also Ref. [20]), but flipping the sign of β_{ST} .

First, we review the work of Refs. [18,19]. Assuming a ST theory of the type discussed in this paper, the Friedmann-Robertson-Walker evolution of the scalar field is described by [18,19]

$$\frac{2}{3 - \varphi^2} \varphi'' + (1 - w)\varphi' = -(1 - 3w)\bar{\alpha}(\varphi). \quad (\text{A1})$$

Here, $\varphi \equiv \psi\sqrt{4\pi G}$, primes indicate dimensionless derivatives with respect to a time variable τ such that $d\tau = H_E(t_E)dt_E$, or simply $\tau = \ln a_E(t_E) + \text{const}$, where a_E , H_E , and t_E are the expansion parameter, the Hubble expansion rate, and the cosmological time in the Einstein frame respectively. Also, $\bar{\alpha}(\varphi) = \partial \ln(1/\phi(\varphi))/\partial\varphi \equiv \partial a(\varphi)/\partial\varphi$, but in the theories of interest to us, $\bar{\alpha}(\varphi) = \beta_{ST}\varphi$. Finally, in this equation, $w = p/\rho$ is the usual cosmological EoS parameter, where p and ρ are the pressure and density of the cosmic fluid respectively, i.e., $w = -1, 1/3$, or 0 during the inflationary, radiation, and matter eras respectively. Clearly, Eq. (A1) can intuitively be understood as a particle with (velocity-dependent) mass $m = 2/(3 - \varphi^2)$ moving in a potential, $a(\varphi)$, with a "friction" term $(1 - w)\varphi'$.

During the inflationary era ($w = -1$), Eq. (A1) admits a solution $\varphi = \varphi_0 + \sqrt{3}\tau$, as can be checked explicitly³ by replacing it into Eq. (A1) multiplied by $3 - \varphi^2$. We now show that, during inflation, this solution is indeed an attractor at linear order. To this purpose, let us write $\varphi = \sqrt{3}\tau + \delta\varphi$ (where we have absorbed φ_0 in $\delta\varphi$). At linear order in $\delta\varphi$, Eq. (A1) yields

$$\delta\varphi'' - 6(1 + 2\beta_{ST}\tau)\delta\varphi' = 0, \quad (\text{A2})$$

which in turn gives

$$\begin{aligned} \delta\varphi(\tau) = \varphi_1 + \frac{\sqrt{\frac{\pi}{2}}e^{-\frac{3}{2\beta_{ST}}(\sqrt{3}\varphi_2 - 3)}}{6\sqrt{-\beta_{ST}}} \\ \times \left[-\text{Erf}\left(\sqrt{\frac{3}{-2\beta_{ST}}}(2\beta_{ST}\tau + 1)}\right) + \text{Erf}\left(\sqrt{\frac{3}{-2\beta_{ST}}}\right) \right] \end{aligned} \quad (\text{A3})$$

where $\text{Erf}[\cdot]$ is the error function and we have chosen the initial conditions $\varphi_1 = \varphi(0)$ and $\varphi_2 = \varphi'(0)$, so as to match respectively the value of $\varphi = \sqrt{3}\tau + \delta\varphi$ and that of its first time derivative at $\tau = 0$. Because $\text{Erf}(x) \rightarrow 1$ as $x \rightarrow \infty$, it is clear that $\delta\varphi$ goes asymptotically to a constant; hence the asymptotic solution becomes $\varphi = \sqrt{3}\tau + \delta\varphi \approx \varphi_0 + \sqrt{3}\tau$.

During the radiation era, $w = 1/3$ and the general solution to Eq. (A1) is [18,19]

$$\varphi = \varphi_\infty - \sqrt{3} \ln [K e^{-\tau} + (1 + K^2 e^{-2\tau})^{1/2}] \quad (\text{A4})$$

where φ_∞ and K are integration constants. This shows that a nonzero initial value of φ is damped away in the radiation era. This can also be seen by solving Eq. (A1) under the approximation $\varphi' \approx 0$, which yields $\varphi'' + \varphi' = 0$ and thus $\varphi \approx \varphi_\infty - K e^{-\tau}$.

Finally, in the matter era $w = 0$, the solution $\varphi = \varphi_0 + \sqrt{3}\tau$ to Eq. (A1) is still an attractor. To prove that this is so, we write $\varphi = \sqrt{3}\tau + \delta\varphi$ (where again we have absorbed φ_0 in $\delta\varphi$), which together with Eq. (A1) yields

$$\delta\varphi'' - 3(1 + \beta_{ST}\tau)\delta\varphi' = 0 \quad (\text{A5})$$

at linear order in $\delta\varphi$. Solving this equation, one obtains

$$\begin{aligned} \delta\varphi(\tau) = \varphi_1 + \frac{\sqrt{\frac{\pi}{2}}e^{-\frac{3}{2\beta_{ST}}(\sqrt{3}\varphi_2 - 3)}}{3\sqrt{-\beta_{ST}}} \\ \times \left[-\text{Erf}\left(\sqrt{\frac{3}{-2\beta_{ST}}(\beta_{ST}\tau + 1)}\right) + \text{Erf}\left(\sqrt{\frac{3}{-2\beta_{ST}}}\right) \right], \end{aligned} \quad (\text{A6})$$

where $\varphi_1 = \varphi(0)$ and $\varphi_2 = \varphi'(0)$ are the two constants of integration, chosen to match respectively the value of

³In fact, this is a solution for any w .

$\varphi = \sqrt{3}\tau + \delta\varphi$ and that of its first time derivative at $\tau = 0$. Again, this shows that $\varphi = \varphi_0 + \sqrt{3}\tau$ is a linear attractor for Eq. (A1). Because in the radiation era preceding the matter era φ is exponentially small, we can assume $\varphi_1 = \varphi(0) \approx 0$ and $\varphi_2 = \varphi'(0) \approx 0$ (setting $\tau = 0$ at the end of the radiation era). Inserting these conditions into Eq. (A6), we obtain $\varphi(\tau_{\text{now}}) = \sqrt{3}\tau_{\text{now}} + \delta\varphi(\tau_{\text{now}}) \approx 16$ at the present time $\tau_{\text{now}} \approx 10$ [18,19] for $\beta_{\text{ST}} = -4.5$.

With the present value of the scalar field at hand, we can now study what effect this has on Solar System tests. First, we relate the ppN parameter, γ_{ppN} , to $\bar{\alpha}$ via [19]

$$1 - \gamma_{\text{ppN}} = \frac{2\bar{\alpha}^2}{1 + \bar{\alpha}^2} = \frac{2\beta_{\text{ST}}^2\varphi^2}{1 + \beta_{\text{ST}}^2\varphi^2}. \quad (\text{A7})$$

In GR, $1 - \gamma_{\text{ppN}} = 0$ and Solar System observations have placed stringent bounds on this quantity: $|1 - \gamma_{\text{ppN}}| < 2 \times 10^{-3}$ [19]. Evaluating $1 - \gamma_{\text{ppN}}$ at the present time for $\beta_{\text{ST}} = -4.5$ (i.e., $\varphi = \varphi_{\text{now}} \approx 16$), we obtain $1 - \gamma_{\text{ppN}} \approx 2$, which is clearly in violation of Solar System experiments. In fact, since φ will continue to linearly grow ever larger, γ_{ppN} will continue to approach 2 as

$$1 - \gamma_{\text{ppN}} \approx 2 \left[1 - \frac{1}{3\beta_{\text{ST}}^2\tau^2} + \mathcal{O}\left(\frac{1}{\tau^4}\right) \right]. \quad (\text{A8})$$

Note, however, that a different functional form for $\bar{\alpha}(\varphi)$ and/or the presence of a suitable potential for the scalar field may lead to different behavior, but such issues have not yet been fully explored (but see Ref. [20] for some work in this direction).

APPENDIX B: RELATIONSHIP BETWEEN \mathcal{N}_u AND \mathcal{N}_e

The useful cycles of phase, \mathcal{N}_u , and the effective cycles of phase, \mathcal{N}_e , can be related (in the limit of small

dephasings) by a simple calculation. Via this calculation, in this Appendix we show that the relationship between these two quantities is dependent only on the PN order of the difference in phase, focusing only on the inspiral phase with the PN approximation.

Consider two GW signals whose phases differ only by a ppE term of the form βu^b . That is, $\Phi_1 = \Phi_{\text{GR}}$ and $\Phi_2 = \Phi_{\text{GR}} + \beta u^b$. We can then write \mathcal{N}_u as

$$\mathcal{N}_u = \frac{\text{SNR}^2}{\int \frac{h_c^2}{S_n(f)} \frac{1}{N(f)} d \ln f} - \frac{\text{SNR}^2}{\int \frac{h_c^2}{S_n(f)} \frac{1}{N(f)+\delta} d \ln f}, \quad (\text{B1})$$

where $\delta = \Phi_1 - \Phi_2 = \beta u^b$ in this case. In the limit that δ is small, we can expand this expression to get

$$\mathcal{N}_u = -\text{SNR}^2 \frac{\int \frac{h_c^2}{S_n(f)} \frac{\delta}{N_{\text{GR}}^2} d \ln f}{\left(\int \frac{h_c^2}{S_n(f)} \frac{1}{N_{\text{GR}}} d \ln f \right)^2}. \quad (\text{B2})$$

Given the form of δ , it is clear that \mathcal{N}_u can be written as

$$\mathcal{N}_u = \beta g(b), \quad (\text{B3})$$

where $g(b)$ is the function defined by performing the integrations in Eq. (B2).

Similarly, we can write the effective cycles of phase

$$\mathcal{N}_e = \frac{\left(\int \frac{h_c^2}{S_n(f)} \delta^2 d \ln f \right)^{1/2}}{2\pi \text{SNR}} = \beta h(b), \quad (\text{B4})$$

where $h(b)$ encapsulates the b dependence of the integral in the above equation.

Taking the ratio of these two expressions, it is also clear that all β dependence cancels exactly, and the two are related by some complicated function in b , the exponent parameter.

-
- [1] LIGO, <http://www.ligo.caltech.edu>.
[2] A. Abramovici, W. E. Althouse, R. W. Drever, Y. Gursel, S. Kawamura *et al.*, *Science* **256**, 325 (1992).
[3] B. Abbott *et al.* (LIGO Scientific Collaboration), *Rep. Prog. Phys.* **72**, 076901 (2009).
[4] VIRGO, <http://www.virgo.infn.it>.
[5] A. Giazotto, *Nucl. Instrum. Methods Phys. Res., Sect. A* **289**, 518 (1990).
[6] K. Kuroda (LCGT Collaboration), *Classical Quantum Gravity* **27**, 084004 (2010).
[7] N. Yunes and X. Siemens, *Living Rev. Relativity* **16**, 9 (2013).
[8] D. Psaltis, [arXiv:astro-ph/0501234](https://arxiv.org/abs/astro-ph/0501234).
[9] I. H. Stairs, *Living Rev. Relativity* **6**, 5 (2003).
[10] T. Damour and J. H. Taylor, *Phys. Rev. D* **45**, 1840 (1992).
[11] M. Kramer and N. Wex, *Classical Quantum Gravity* **26**, 073001 (2009).
[12] P. C. Freire, N. Wex, G. Esposito-Farese, J. P. Verbiest, M. Bailes, B. A. Jacoby, M. Kramer, I. H. Stairs, J. Antoniadis, and G. H. Janssen, *Mon. Not. R. Astron. Soc.* **423**, 3328 (2012).
[13] T. Damour and G. Esposito-Farese, *Classical Quantum Gravity* **9**, 2093 (1992).
[14] T. Damour and G. Esposito-Farese, *Phys. Rev. Lett.* **70**, 2220 (1993).

- [15] E. Barausse, C. Palenzuela, M. Ponce, and L. Lehner, *Phys. Rev. D* **87**, 081506 (2013).
- [16] T. Damour and G. Esposito-Farese, *Phys. Rev. D* **54**, 1474 (1996).
- [17] C. Palenzuela, E. Barausse, M. Ponce, and L. Lehner, *Phys. Rev. D* **89**, 044024 (2014).
- [18] T. Damour and K. Nordtvedt, *Phys. Rev. D* **48**, 3436 (1993).
- [19] T. Damour and K. Nordtvedt, *Phys. Rev. Lett.* **70**, 2217 (1993).
- [20] L. Järvi, P. Kuusk, and M. Saal, *Phys. Rev. D* **78**, 083530 (2008).
- [21] M. Shibata, K. Taniguchi, H. Okawa, and A. Buonanno, *Phys. Rev. D* **89**, 084005 (2014).
- [22] L. Sampson, N. Cornish, and N. Yunes, *Phys. Rev. D* **89**, 064037 (2014).
- [23] L. Lindblom, B. J. Owen, and D. A. Brown, *Phys. Rev. D* **78**, 124020 (2008).
- [24] T. Damour, B. R. Iyer, and B. Sathyaprakash, *Phys. Rev. D* **62**, 084036 (2000).
- [25] L. Baiotti, T. Damour, B. Giacomazzo, A. Nagar, and L. Rezzolla, *Phys. Rev. D* **84**, 024017 (2011).
- [26] K. Yagi, *Phys. Rev. D* **89**, 043011 (2014).
- [27] D. Gerosa, R. O’Shaughnessy, M. Kesden, E. Berti, and U. Sperhake, *Phys. Rev. D* **89**, 124025 (2014).
- [28] N. Yunes and F. Pretorius, *Phys. Rev. D* **80**, 122003 (2009).
- [29] L. Sampson, N. Cornish, and N. Yunes, *Phys. Rev. D* **87**, 102001 (2013).
- [30] M. Fierz, *Helv. Phys. Acta* **29**, 128 (1956).
- [31] P. Jordan, *Z. Phys.* **157**, 112 (1959).
- [32] C. Brans and R. Dicke, *Phys. Rev.* **124**, 925 (1961).
- [33] C. M. Will, *Living Rev. Relativity* **9**, 3 (2006).
- [34] B. Bertotti, L. Iess, and P. Tortora, *Nature (London)* **425**, 374 (2003).
- [35] T. Damour and G. Esposito-Farese, *Phys. Rev. D* **58**, 042001 (1998).
- [36] D. M. Eardley, *Astrophys. J. Lett.* **196**, L59 (1975).
- [37] T. Damour and G. Esposito-Farese, *Phys. Rev. D* **53**, 5541 (1996).
- [38] S. Mirshekari and C. M. Will, *Phys. Rev. D* **87**, 084070 (2013).
- [39] C. M. Will and H. W. Zaglauer, *Astrophys. J.* **346**, 366 (1989).
- [40] L. Blanchet, S. L. Detweiler, A. Le Tiec, and B. F. Whiting, *Phys. Rev. D* **81**, 064004 (2010).
- [41] L. Blanchet, S. L. Detweiler, A. Le Tiec, and B. F. Whiting, *Phys. Rev. D* **81**, 084033 (2010).
- [42] L. Blanchet, S. Detweiler, A. Le Tiec, and B. F. Whiting, *Fund. Theor. Phys.* **162**, 415 (2011).
- [43] N. Yunes, K. Arun, E. Berti, and C. M. Will, *Phys. Rev. D* **80**, 084001 (2009).
- [44] K. Chatziioannou, N. Yunes, and N. Cornish, *Phys. Rev. D* **86**, 022004 (2012).
- [45] L. E. Kidder, *Phys. Rev. D* **52**, 821 (1995).
- [46] E. Poisson and C. Will, *Gravity: Newtonian, Post-Newtonian, Relativistic* (Cambridge University Press, Cambridge, England, 2014).
- [47] D. M. Eardley, D. L. Lee, and A. P. Lightman, *Phys. Rev. D* **8**, 3308 (1973).
- [48] C. M. Will, *Theory and Experiment in Gravitational Physics*, edited by C. M. Will (Cambridge University Press, Cambridge, England, 1993), p. 396.
- [49] C. M. Will, *Phys. Rev. D* **50**, 6058 (1994).
- [50] A. Nishizawa, A. Taruya, K. Hayama, S. Kawamura, and M.-a. Sakagami, *Phys. Rev. D* **79**, 082002 (2009).
- [51] K. Hayama and A. Nishizawa, *Phys. Rev. D* **87**, 062003 (2013).
- [52] A. Nishizawa and K. Hayama, *Phys. Rev. D* **88**, 064005 (2013).
- [53] P. Horava, A. Mohd, C. M. Melby-Thompson, and P. Shawhan, *Gen. Relativ. Gravit.* **46**, 1720 (2014).
- [54] C. M. Bender and S. A. Orszag, *Advanced Mathematical Methods for Scientists and Engineers I, Asymptotic Methods and Perturbation Theory* (Springer, New York, 1999).
- [55] C. Cutler and É. E. Flanagan, *Phys. Rev. D* **49**, 2658 (1994).
- [56] L. Blanchet, G. Faye, B. R. Iyer, and B. Joguet, *Phys. Rev. D* **65**, 061501 (2002).
- [57] N. Cornish, L. Sampson, N. Yunes, and F. Pretorius, *Phys. Rev. D* **84**, 062003 (2011).
- [58] aLIGO noise curves, <https://dcc.ligo.org/LIGO-T0900288/public>.
- [59] J. M. Dickey *et al.*, *Ann. Math. Stat.* **42**, 204 (1971).
- [60] T. Littenerbg, Ph.D. thesis, Montana State University, 2010.
- [61] A. Klein, N. Cornish, and N. Yunes, *Phys. Rev. D* **88**, 124015 (2013).
- [62] K. Chatziioannou, A. Klein, N. Yunes, and N. Cornish, *Phys. Rev. D* **88**, 063011 (2013).
- [63] K. Chatziioannou, N. Cornish, A. Klein, and N. Yunes, *Phys. Rev. D* **89**, 104023 (2014).
- [64] K. Chatziioannou, N. Cornish, A. Klein, and N. Yunes, arXiv:1402.3581.
- [65] A. Stavridis and C. Will, *J. Phys. Conf. Ser.* **228**, 012049 (2010).
- [66] K. Yagi and T. Tanaka, *Phys. Rev. D* **81**, 064008 (2010).
- [67] K. Yagi and T. Tanaka, *Prog. Theor. Phys.* **123**, 1069 (2010).
- [68] J. Clark, A. Bauswein, L. Cadonati, H. T. Janka, C. Pankow, and N. Stergioulas, *Phys. Rev. D* **90**, 062004 (2014).
- [69] E. Berti, J. Gair, and A. Sesana, *Phys. Rev. D* **84**, 101501 (2011).
- [70] W. Del Pozzo, T. G. F. Li, M. Agathos, C. Van Den Broeck, and S. Vitale, *Phys. Rev. Lett.* **111**, 071101 (2013).
- [71] Einstein Telescope, <http://www.et-gw.eu>.
- [72] K. Taniguchi, M. Shibata, and A. Buonanno, arXiv:1410.0738.
- [73] T. Damour, A. Nagar, and L. Villain, *Phys. Rev. D* **85**, 123007 (2012).
- [74] L. Wade, J. D. E. Creighton, E. Ochsner, B. D. Lackey, B. F. Farr, T. B. Littenberg, and V. Raymond, *Phys. Rev. D* **89**, 103012 (2014).